

VECTOR MAGNETIC FIELD IMAGING WITH QUANTUM DIAMOND
SENSOR



NAPOOM THOOPPANOM

A Thesis Submitted in Partial fulfillment of the Requirements for the

Degree of Master of Science in Physics

Suranaree University of Technology

Academic Year 2024

การถ่ายภาพเวกเตอร์สนามแม่เหล็กด้วยควอนตัมเซนเซอร์เพชร



วิทยานิพนธ์นี้เป็นส่วนหนึ่งการศึกษาตามหลักสูตรปริญญาวิทยาศาสตรมหาบัณฑิต

สาขาฟิสิกส์

มหาวิทยาลัยเทคโนโลยีสุรนารี

ปีการศึกษา 2567

VECTOR MAGNETIC FIELD IMAGING WITH QUANTUM DIAMOND SENSOR

Suranaree University of Technology has approved this thesis submitted in partial fulfillment of the requirements for a Master's Degree.

Thesis Examining Committee



(Assoc. Prof. Dr. Panomsak Meemon)

Chairperson



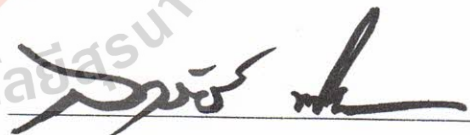
(Dr. Sorawis Sangtawesin)

Member (Thesis advisor)



(Dr. Warintorn Sreethawong)

Member



(Asst. Prof. Dr. Ekkarat Pongophas)

Member



(Assoc. Prof. Dr. Yupaporn Ruksakulpiwat)

Vice Rector for Academic Affairs

and Quality Assurance



(Prof. Dr. Santi Maensiri)

Dean of Institute of Science

ณภูมิ ฐูปพนม : การถ่ายภาพสนามแม่เหล็กด้วยควอนตัมเซนเซอร์เพชร (VECTOR MAGNETIC FIELD IMAGING WITH QUANTUM DIAMOND SENSOR) อาจารย์ที่ปรึกษา: อาจารย์ ดร. สรวิต แสงทวีสิน, 48 หน้า

คำสำคัญ: การตรวจจับทางควอนตัม, ตำแหน่งไนโตรเจนที่ว่าง, การตรวจจับสนามแม่เหล็ก

เซนเซอร์ตรวจวัดสนามแม่เหล็กถูกนำมาใช้อย่างแพร่หลายในระบบขนส่ง การสื่อสาร และระบบนำทาง อย่างไรก็ตาม เซนเซอร์ดังกล่าวยังคงมีข้อจำกัดในด้านทิศทางของสนามแม่เหล็กที่สามารถตรวจจับได้ และความไวต่อสนามแม่เหล็กความเข้มต่ำ การตรวจจับทางควอนตัม โดยเฉพาะเทคนิคที่อาศัยศูนย์ตำแหน่งไนโตรเจนว่าง (Nitrogen Vacancy: NV center) ในเพชร สามารถช่วยลดข้อจำกัดดังกล่าวได้อย่างมีประสิทธิภาพ โดย NV center ซึ่งเป็นตำหนิชนิดหนึ่งในโครงสร้างของเพชร มีสมบัติในการตรวจวัดสนามแม่เหล็กได้อย่างแม่นยำภายใต้สภาวะแวดล้อมปกติ จึงเหมาะสมอย่างยิ่งสำหรับการประยุกต์ใช้งานด้านการตรวจวัดหลากหลายรูปแบบ

งานวิจัยนี้ นำ NV center มาใช้ในการตรวจวัดสนามแม่เหล็กเชิงเวกเตอร์ (Vector Magnetometry) และการสร้างแผนที่ของสนามแม่เหล็กที่ไม่ทราบค่า โดยจำลองสถานการณ์ที่มีแม่เหล็กเคลื่อนที่อยู่เหนือพื้นผิวของเพชร การทดลองทั้งสองส่วนใช้ลำดับการตรวจวัดเรโซแนนซ์แม่เหล็กที่ตรวจจับด้วยแสง (Optically Detected Magnetic Resonance: ODMR) ในการตรวจจับสัญญาณ วิธีการทดลองอาศัยโปรแกรมสแกนความถี่ที่มีความละเอียด 26 เมกะเฮิรตซ์ โดยใช้เวลา 5 วินาทีต่อข้อมูล 200 จุด และใช้ของ Quantum Diamond Sensor (QDS) ตามที่ Bucher และคณะ (2019) ได้เสนอไว้การคำนวณสนามแม่เหล็กดำเนินการโดยอิงจาก Hamiltonian ของ NV center เพื่อนำมาวิเคราะห์ขนาดและทิศทางของสนามแม่เหล็กจากสัญญาณ ODMR ซึ่งค่าความเข้มที่ได้แสดงถึงอิทธิพลของสนามแม่เหล็กที่กระทำต่อแกนของ NV center แต่ละทิศทาง ในขณะที่ข้อมูลทิศทางบ่งชี้ถึงมุมระหว่างสนามแม่เหล็กกับแกนของ NV center แต่ละแกน วิธีการดังกล่าวสามารถแสดงให้เห็นทิศทางของสนามแม่เหล็กได้โดยการสร้างพื้นผิวตามแนวแกนของ NV center ซึ่งจุดตัดของพื้นผิวเหล่านี้สะท้อนถึงทิศทางของสนามแม่เหล็กที่ตำแหน่งของ NV center

ในการวิเคราะห์สนามแม่เหล็กเชิงเวกเตอร์นั้นไม่เพียงแต่สามารถคำนวณขนาดและทิศทางของสนามแม่เหล็กได้เท่านั้น แต่ยังสามารถแยกความแตกต่างของสัญญาณ ODMR ที่มีรูปแบบใกล้เคียงกันได้ถึงสองกรณี รวมถึงสามารถแยกความแตกต่างของมุมเล็ก ๆ ของสัญญาณ ODMR ได้ อีกสองกรณี สำหรับการทดลองสร้างแผนที่สนามแม่เหล็กที่ความสูง 1.7 เซนติเมตรเหนือพื้นผิวเพชร ในทิศเหนือ พบว่าสามารถแสดงภาพสนามแม่เหล็กเชิงเวกเตอร์และสนามแม่เหล็กเชิง gradient ใน

ทิศ x , y และ z บนระนาบ xy ได้อย่างชัดเจน โดยผลลัพธ์สอดคล้องกับการกระจายของสนามแม่เหล็กตามทฤษฎี นอกจากนี้ยังมีการศึกษาสนามแม่เหล็กในระดับความสูงที่ต่างกันสามตำแหน่งเหนือพื้นผิวเพชร ซึ่งแสดงให้เห็นถึงการเปลี่ยนแปลงของสนามแม่เหล็กในแต่ละระดับ โดย gradient ของสนามแม่เหล็กในทิศ x และ y มีแนวโน้มเพิ่มขึ้นอย่างมีนัยสำคัญ ขณะที่สนามแม่เหล็กในทิศ z มีความเข้มเพิ่มขึ้นบริเวณศูนย์กลาง แต่กลับลดลงอย่างชัดเจนบริเวณโดยรอบ อันเป็นผลจากการพลิกทิศของสนามแม่เหล็กไปยังทิศทางของขั้วใต้ นอกจากนี้ ยังมีการแสดงภาพเวกเตอร์ของสนามแม่เหล็กในระนาบ xz และ yz ซึ่งให้ผลลัพธ์สอดคล้องกับข้อมูลจากการทดลองก่อนหน้า



สาขาวิชาฟิสิกส์
ปีการศึกษา 2567

ลายมือชื่อนักศึกษา ณัฐมิ
ลายมือชื่ออาจารย์ที่ปรึกษา [Signature]

NAPOOM THOOPANOM : VECTOR MAGNETIC FIELD IMAGING WITH QUANTUM DIAMOND SENSOR. THESIS ADVISOR : SORAWIS SANGTAWESIN, PhD. 48 PP.

Keywords: quantum sensing, NV center, magnetic field sensing

Magnetic field sensors are frequently used in transportation, communication, and navigation applications. The constraints of the sensors are the direction of the magnetic field and low magnetic field strength. Quantum sensing, especially those utilizing nitrogen vacancy (NV) centers in diamonds, can overcome the constraints. The NV center, a defect in diamond, is an efficient sensor for magnetic fields and functions under ambient conditions, providing it to be suitable for many sensing applications.

This thesis uses the NV center for vector magnetometry and the mapping of unknown magnetic fields, with a moving magnet perspective above the diamond. Both experiments employ optically detected magnetic resonance (ODMR) sequences for signal detection. Their methodology employs a sweep program with a resolution of 26 MHz, scanning at a rate of 5 seconds for every 200 data points, and utilizes a Quantum Diamond Sensor (QDS) configuration as described by Bucher et al. (2019). Magnetic field calculations are obtained from the NV center Hamiltonian to compute the amplitude and orientation of the magnetic field based on the ODMR signal. The computed magnitude indicates the magnetic field influencing each NV axis, while the orientation indicates the calculation of the angle between the magnetic field and each NV axis. This method enables the viewing of magnetic field direction by generating surfaces along the NV axes, which correspond to the magnetic field orientation at the NV center through their intersections with the surfaces.

For vector magnetometry, the analysis not only computes the magnitude and direction of the magnetic field but also distinguishes 2 differences between similar ODMR signal shapes and 2 small angles of ODMR signal. In the mapping experiment above the diamond 1.7 cm in the north pole direction, the vector field and gradient field in the x, y, and z directions are visualized on the xy plane, showing good agreement with the theoretical magnetic field distribution. Additionally, the NV center

examines the magnetic field at three different heights above the diamond, illustrating magnetic field changes at each level. As a result, the magnetic field gradient in the x and y directions increases significantly, whereas the magnetic field in the z direction increases at the center area but decreases considerably around the center due to flipping direction to the south pole. In addition, there are vector magnetic field visualizations in the xz and yz planes, which is consistent with previous results.



School of Physics
Academic Year 2024

Student's signature ณภัณี
Advisor's signature [Signature]

ACKNOWLEDGEMENTS

I wish to express my deepest gratitude to my esteemed advisor, Dr. Sorawis Sangtawesin, whose exceptional guidance and steadfast support have been invaluable throughout my master's studies. His mentorship not only provided critical direction in my research but also offered me the opportunity to engage in stimulating academic activities and projects, enriching my learning experience and preparing me for doctoral degree.

I am profoundly thankful to the distinguished members of thesis and proposal committees—Professor Dr. Joewono Widjaja, Associate Professor Panomsak Meemon, Dr. Warintorn Sreethawong, and Assistant Professor Dr. Ekkarat Pongophas, —whose insightful comments and constructive feedback have greatly contributed to the refinement of thesis.

I also extend my sincere appreciation to the OCT and QLAB members for their valuable guidance and support. My heartfelt thanks go to the Development Program in Science and Technology (DPST) for the funding provided during my degree, and to the NSRF, through the Program Management Unit for Human Resources & Institutional Development, Research and Innovation [grant number B39G670018], for funding this research endeavor.

Finally, I am grateful to my family and friends for their support and encouragement throughout my academic journey. Their confidence in my abilities has been a driving force in the successful completion of my studies. Each contribution has played a significantly, shaping my educational experience.

Napoom Thooppanom

CONTENTS

	Page
ABSTRACT IN THAI.....	I
ABSTRACT IN ENGLISH.....	III
ACKNOWLEDGEMENTS.....	V
CONTENTS.....	VI
LIST OF TABLES.....	VIII
LIST OF FIGURES.....	IX
CHAPTER	
I INTRODUCTION.....	1
1.1 Introduction.....	1
1.2 Research objective.....	2
1.3 Scope of thesis.....	2
1.4 Outline of thesis.....	3
II LITERATURE REVIEWS	4
2.1 Quantum bits or Qubit.....	4
2.2 Nitrogen Vacancy (NV) center.....	5
2.2.1 NV center.....	5
2.2.2 Energy level diagram.....	6
2.2.3 Zeeman splitting effect on NV center.....	7
2.2.4 Hamiltonian of Nitrogen Vacancy center.....	8
2.2.5 Application of utilizing NV center.....	9
III RESEARCH METHODOLOGY.....	10
3.1 Quantum Diamond Spectrometer (QDS).....	10
3.1.1 Optical system.....	11
3.1.2 Electronics system.....	12

CONTENTS (Continued)

	Page
3.2 Pulse sequence.....	13
3.2.1 Optically Detected Magnetic Resonance (ODMR).....	13
3.3 Microwave generator	16
3.4 Determining magnetic field magnitudes and orientations.....	16
3.4.1 Signal detection process.....	17
3.4.2 Program.....	17
3.4.2.1 Sweeping function.....	17
3.4.2.2 Sweeping parameters.....	18
3.4.2.3 ODMR parameters.....	18
3.4.3 Magnetic field calculation.....	18
3.4.4 Experimental workflow.....	23
IV RESULTS AND DISCUSSION.....	25
4.1 Validation measurement.....	25
4.2 Resolution test.....	27
4.2.1 Magnetic field from different directions with similar ODMR signal	27
4.2.2 ODMR signal with small angle differences.....	29
4.3 NV center as a magnetic field scanner.....	31
4.4 Setup for magnetometry.....	34
4.5 Magnetic field strength above the NV center at 1.7 cm.....	35
4.6 Magnetic field direction above the NV center at 1.7 cm.....	37
4.7 Magnetic field at 3 different heights.....	38
V CONCLUSION.....	42
REFERENCES.....	44
CURRICULUM VITAE.....	48

LIST OF TABLES

Table	Page
2.1 Pulse duration for Pulsed ODMR.....	15



LIST OF FIGURES

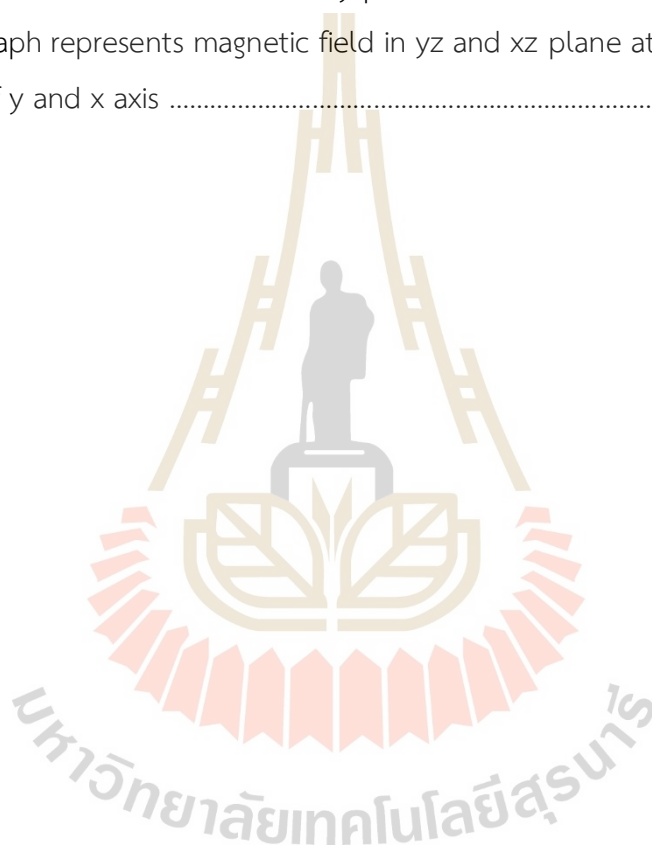
Figure		Page
2.1	Bloch sphere is a demonstration of a pure state with θ and ϕ angle	4
2.2	A nitrogen-vacancy (NV) center in diamond is formed by an N substitution and a nearest neighbor vacancy	5
2.3	The NV center energy level consists of a ground state at $m_s = 0$ and degenerated states at $m_s = \pm 1$	7
2.4	When magnetic field is applied, degenerate energy levels of $m_s = \pm 1$ are split with distance with Eq 2.....	7
3.1	Quantum Diamond Spectrometer (QDS) schematic	12
3.2	Electronic diagram for controlling microwave	13
3.3	OD-ESR sequence is designed to find the position of an energy level of a NV for control sequence	15
3.4	The full width half maximum (FWHM) of system is 26 MHz with using the first dip of Zeeman 4 splitting.....	16
3.5	Sweeping program is designed by Qtdesigner	18
3.6	A NV axis and magnetic field in the system. Angle between magnetic field and a NV axis is called alpha and calculated by Eq. 4.....	19
3.7	The two cones represent possible magnetic field direction and 2 orthogonal vectors constraining are perpendicular to NV axis and each other	20
3.8	Transformation from cartesian coordinate to spherical coordinate with using trigonometry	22
3.9	The 4 orientation of NV center senses magnetic field in the specific direction and create cones along NV axes	23
3.10	3D and 2D graph represent that answer sets of 4 NV axes are not unique and have interceptions	24

LIST OF FIGURES (Continued)

Figure	Page
4.1	Result from magnetic field calculation represents comparison between real signal, simulated signal and projected cone 26
4.2	Two ODMR signals with similar shape acquired when θ and ϕ is set to 150°, 50° (red), and 160°, 70° (blue)..... 28
4.3	The calculation result of the first special case. The blue and red curves are the calculated results of NV axes that sense magnetic field from the blue and red ODMR signal respectively 28
4.4	The two ODMR signals with small difference acquired when θ and ϕ is set to 68°,156° (red), and 70°, 165° (blue)..... 30
4.5	The two ODMR signals with small differences acquired when θ and ϕ is set to 70°, 157° (red), and 70°, 155° (blue)..... 31
4.6	The magnetic field in scanning-NV perspective is observed by sensor 32
4.7	The picture a), b), c), d), e), and f) represent magnet is moved at the different position and NV center sense different magnetic field direction as a position in moving-magnet and scanning-NV perspective. 33
4.8	The new setup without magnet on dial has a plate for moving magnet plane with magnet on the top of plate..... 34
4.9	The plate is attached by graph paper. The graph shows detection area for experiment with setting the center of the system at 0 and border from 2.5 to -2.5 in x and y direction 35
4.10	In this figure represent magnetic field gradient above the NV center at 1.7 cm. Each picture presents magnetic field in component xyz 36
4.11	Vector field presents the distribution of magnetic field in x and y direction in xy plane at 1.7 cm 37

LIST OF FIGURES (Continued)

Figure		Page
4.12	The graph represents magnetic field gradient at total magnetic field, b_x , b_y and b_z at different height above the NV center.....	40
4.13	The graph represents vector field of magnetic field at the different heights above the NV center in xy plane	41
4.14	The graph represents magnetic field in yz and xz plane at the central line of y and x axis	41



CHAPTER I

INTRODUCTION

1.1 Introduction

Magnetic field measurement plays a crucial role in human activities such as navigation, medical diagnosis, and material characterization (Li et al., 2022). Nowadays, as technology advances and the need for ever-greater precision grows, magnetic field measurement at the nanoscale is increasingly interesting. Therefore, opportunities are opened up for the new innovation such as quantum sensing to improve magnetic field sensing efficiency.

Quantum sensing uses the highly environmentally sensitive quantum state. When a small perturbation interacts with the quantum state, we can trace back to the perturbation quantity from the changed quantum state. For this reason, quantum state can be used as a powerful sensor. The nitrogen Vacancy (NV) center in diamond is an example of a promising ambient quantum system for magnetometry applications. The NV center is a defect in diamond that comes from nitrogen replacement and vacancy formation. As a result, this structure has C_{3V} symmetry, with spin triplet ground states where the $m_s = \pm 1$ can respond to the magnetic field. For example, using the spin triplet ground state of the NV center, one can demonstrate field measurements around magnetic structures and determine the vector magnetic field (Maertz et al., 2010). Utilizing NV for characterization with nuclear magnetic resonance (NMR) technique detect fluorinated sample with hydrogen and fluorine compound via the NV NMR spectra measurement (DeVience et al., 2015). Using NV center increases accurate detection of lower critical magnetic field in superconductors (Joshi et al., 2019).

Conventional NV center studies typically utilize confocal microscopes for high resolution (Acosta et al., 2009), (Gaebel et al., 2006), (Maertz et al., 2010), (Mamin et al.,

2013), but it is time-consuming and unsuitable for applications reliant on speed or those where magnetic field changes rapidly. In contrast, Quantum Diamond Spectrometers (QDS) (Bucher et al., 2019) present a promising solution by offering rapid measurement capabilities, particularly suited for applications that prioritize speed over spatial resolution, such as large-scale biosensing and magnetometry.

Real-time magnetic field monitoring remains challenging despite significant scientific advancements in recent years. For instance, the frequency-locking method, which uses a lock-in amplifier to track the optically detected magnetic resonance (ODMR) signal from NV centers, has improved sensitivity to $4.1 \mu\text{T}/\text{Hz}$ with a sweeping ratio of up to $50 \mu\text{T}/\text{s}$ (Ambal and McMichael, 2018). Another noteworthy development involves coherent population trapping, which estimates magnetic field variations from the time series of observed photons (Turner et al., 2022). Recently, the microwave frequency-hopping method has been introduced, enhancing ODMR measurement speed compared to traditional sweeping methods (Liu et al., 2024). These techniques demonstrate the scanning narrow frequency around 0.1 – 0.2 GHz and low magnetic field.

In this work, we demonstrate the vector magnetometry and mapping unknown magnetic field through optically detected magnetic resonance (ODMR) sequence. The experiments use an ensemble NV center because of the large number of NV center as sensors. In addition, experiments work with rapid magnetic field detection, which uses sweeping mode in a microwave source.

1.2 Research objectives

- 1.2.1 To demonstrate real-time vector magnetometry using the QDS setup.
- 1.2.2 To determine the direction and magnitude of the magnetic field using NV center.

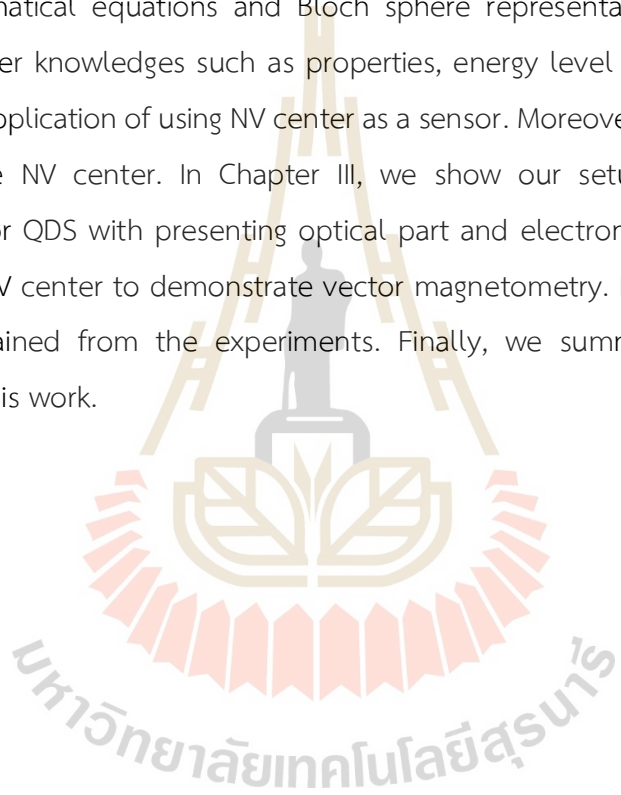
1.3 Scope of thesis

- 1.3.1 We use a type DNV B14 being an ensemble NV center containing NV 4.5 ppm and is grown by chemical vapor deposition (CVD) process.

- 1.3.2 We perform all experiments in ambient condition.
- 1.3.3 We use sweep mode of microwave.

1.4 Outline of thesis

This thesis is divided into 5 chapters. Chapter I is the INTRODUCTION consisting of introduction, objective, and scope of thesis. In Chapter II, we describe a brief quantum bit through mathematical equations and Bloch sphere representations. Continuously, we present NV center knowledges such as properties, energy level diagram, Hamiltonian of NV center and Application of using NV center as a sensor. Moreover, we describe a method for studying the NV center. In Chapter III, we show our setup “Quantum Diamond spectrometer” or QDS with presenting optical part and electronics part. In addition, we use ensemble NV center to demonstrate vector magnetometry. In Chapter IV, we discuss the results obtained from the experiments. Finally, we summarize our findings and comments on this work.



CHAPTER II

LITERATURE REVIEW

In this section, we describe the brief qubit knowledge with equation and Bloch sphere representation. We give the fundamental knowledge of the NV center consisting of properties of the NV center, energy level of the NV center, Zeeman effects on the NV center, Hamiltonian of the NV center and application of utilizing the NV center as a magnetic field sensor.

2.1 Quantum bit

Quantum bit, or qubit, is a fundamental unit in a quantum processor. Unlike the classical bit, which has only existed in one of two binary states (0 or 1), the qubit exists in a superposition of both states simultaneously. As a result, this unique property allows qubits to process calculations more efficiently than classical bits.

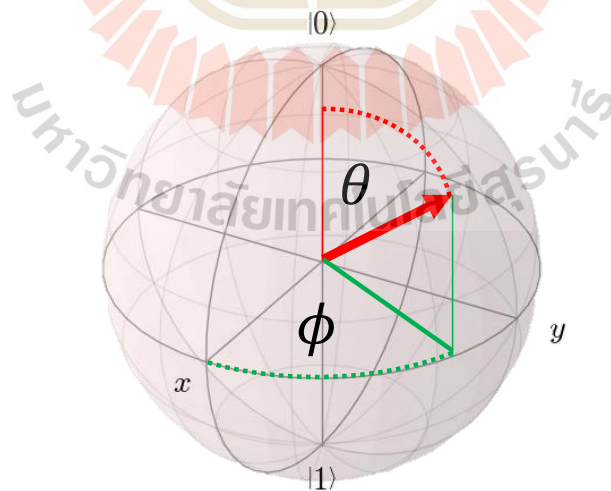


Figure 2.1 The Bloch sphere is a demonstration of a pure state with θ and ϕ angles. The angles θ and ϕ indicate the direction of the magnetic field relative to the NV center in a diamond.

Qubit can be mathematically represented by Eq. 1, as shown below, and can be visualized using a Bloch sphere.

$$|\Psi\rangle = \cos\left(\frac{\theta}{2}\right)|0\rangle + e^{i\phi}\sin\left(\frac{\theta}{2}\right)|1\rangle \quad \text{Eq. 1}$$

Where $|\Psi\rangle$ is the state of qubit. $|0\rangle$ and $|1\rangle$ are state 0 and 1, respectively. The Bloch sphere can represent state through defining all parameters in the equation, as visualized in Figure 2.1 θ and ϕ define spherical coordinate on the vertical and horizontal angles of the Bloch sphere and bra-ket defines state 0 and 1 on the Bloch sphere.

2.2 Nitrogen Vacancy (NV) center

2.2.1 NV center

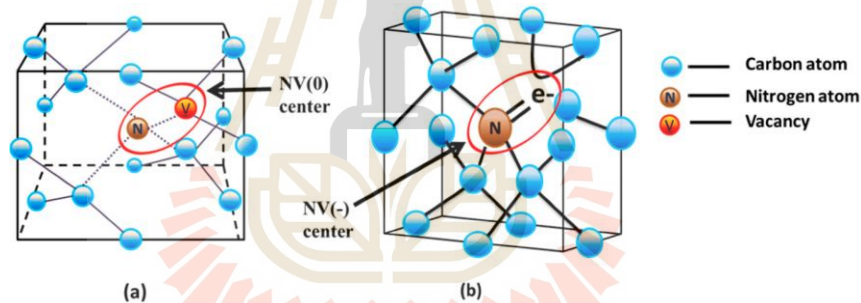


Figure 2.2 A nitrogen-vacancy (NV) center in diamond is formed by an N substitution and a nearest neighbor vacancy (Haque and Sumaiya, 2017).

The NV center refers to a defect found within a diamond lattice. The defect involves the substitution of a carbon atom with a nitrogen atom next to another vacancy in figure 2.2 The NV centers can be classified into two distinct types: neutral NV centers (NV^0) and negatively charged NV centers (NV^-) (Haque and Sumaiya, 2017). The NV^0 and NV^- exhibit singlet and triplet states, respectively. The triplet state, characterized by a spin quantum number $S = 1$, comprises three possible spin orientations: $m_s = 0$, and $m_s = \pm 1$, where the states $m_s = \pm 1$ are degenerated states. Due to unpaired electrons in NV^- , spin-ups and spin-down occur and sense external perturbation. In the field of quantum technology, the utilization of NV^- has garnered considerable attention due to their

potential applications in quantum sensing, particularly in magnetic field detection. Normally, NV center comes in two forms: single NV centers and ensemble NV centers. A single NV center is a single nitrogen defect in a diamond lattice. An ensemble NV center is a group of many NV centers in a diamond sample. For this project, we use an ensemble NV center because the larger number of NV centers in an ensemble increases the number of sensors available, thereby enhancing sensitivity to the level of pT/ $\sqrt{\text{Hz}}$ (Wang Z, et. al., 2022).

2.2.2 Energy level diagram

The ground state and excited state of energy level NV is a triplet state, as shown in figure 2.3. Ground state electrons undergo excitation to an excited state, while following the selection rule. For example, electrons in the ground state with $m_s = 0$ can transition to an excited state with $m_s = 0$, but they are unable to transition to an excited state with $m_s = \pm 1$.

The investigation of NV interaction is conducted by using fluorescence measurement. Typically, ground state electrons with $m_s = 0$ transition to an excited state with $m_s = 0$, and subsequently return to ground state with $m_s = 0$ and simultaneously emit red fluorescence. We can study NV interaction with fluorescence detection.

The electrons can undergo excitation from the $m_s = 0$ state to the degeneracy state $m_s = \pm 1$ with the energy input corresponding to the energy level transition referred to the zero-field splitting, which is 2.87 GHz. After the excitation process, the electrons with $m_s = \pm 1$ have the probability to follow the spin selection rule or relax through a non-radiative metastable state. As a result, the fluorescence contrast decreases due to vanishing electrons in the non-radiative path.

The NV center can be used to detect external magnetic field, which are indicated by the separation of degeneracy level (Zeeman splitting). The energy difference between $m_s = \pm 1$ states is proportional to $2\gamma B_z$ (Eq. 2.), with γ is gyromagnetic ratio of the electron in the NV center having values of 28.024 GHz/T, (Perdriat et al., 2021), and B_z is magnitude of the magnetic field along the z-axis.

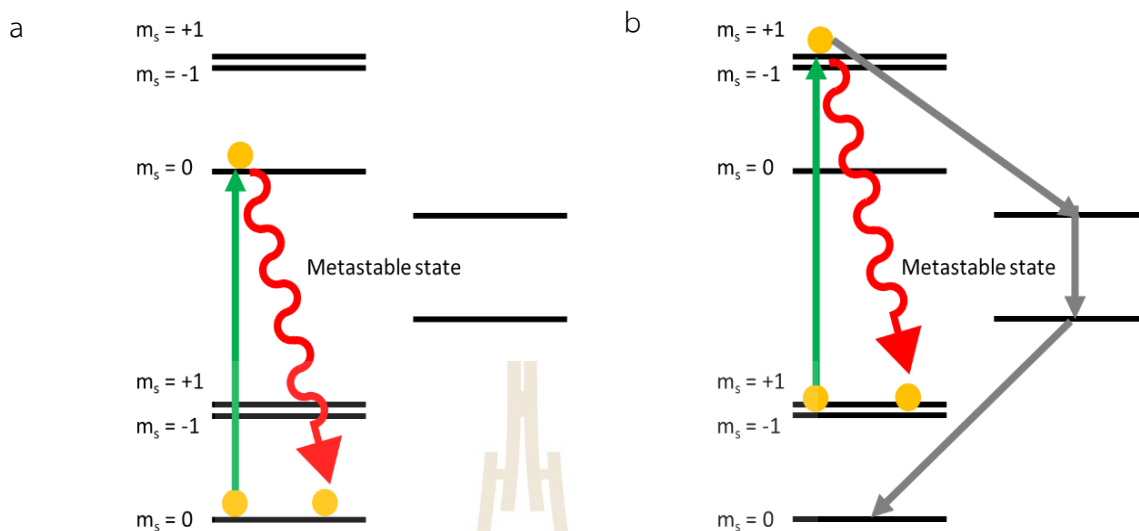


Figure 2.3 The NV center energy level consists of a ground state at $m_s = 0$ and degenerated states at $m_s = \pm 1$. (a) Electrons move according to the selection rule at $m_s = 0$. (b) The electrons excited from the ground state at $m_s = 0$ to the degenerated state at $m_s = \pm 1$ can follow the spin selection rule or go to the metastable state and release non-detectable emission before returning to the ground state $m_s = 0$.

2.2.3 Zeeman splitting effect on NV center



Figure 2.4 When a magnetic field is applied, degenerate energy levels of $m_s = \pm 1$ split with distance with Eq. 2.

We can input an external magnetic field for $m_s = \pm 1$ Zeeman splitting like in figure 2.4. When magnets are added into the system, the NV center has the capability to be a magnetometer in the z axis. As a result, it separates into two dips from a dip from zero-field splitting, representing the $m_s = \pm 1$ transition. They have a distance of

$$\Delta w = 2\gamma B_z \quad \text{Eq. 2}$$

Where Δw is difference of ODMR splitting, γ is gyromagnetic ratio of NV center and B_z is magnitude of the magnetic field along the z-axis.

2.2.4 Hamiltonian of Nitrogen Vacancy center

$$\frac{\hat{H}}{h} = D\hat{S}_z^2 + \gamma_{NV}\vec{B} \cdot \vec{S} \quad \text{Eq. 3}$$

Hamiltonian equation, previously outlined by (Childress et al., 2006, Perdriat et al., 2021), describe the NV center both in the absence and presence of external magnetic field. This equation is defined in a coordinate system where the z-axis aligns with the NV center's [111] crystal axis. The first term is Zero-field splitting where D represents the transition between $m_s = 0$ and $m_s = -1$ or $+1$ due to C_{3v} . The C_{3v} symmetry defines spin states, leading to the NV center having spin $S = 1$ at ground state. In the absence of any external magnetic field, the microwave frequency at 2.87 GHz matching D can excite electrons at $m_s = 0$ to $m_s = 1$ or -1 . The second term is the magnetic field interaction term where γ_{NV} is the electron gyromagnetic ratio, which represents magnetic field effect that perturbs the NV center. When an external magnetic field is applied, the energy level of NV $m_s = \pm 1$ states split from each other, called the Zeeman effect. The parameter γ_{NV} represents the ratio of the frequency shift between energy level $m_s = -1$ and $+1$ energy levels to the magnetic field, resulting from the Zeeman splitting. \vec{B} represents magnetic field in each axis, where the Z axis is along the NV axis and X, Y are perpendicular magnetic field with NV axis.

2.2.5 Application of utilizing NV center

Due to the strongest material and diamond bond, the diamond does not interact with other matters. From the reason, it is non-toxic to the human body. So, NV being hosted in diamond is unique to apply to applications such as biosensor and magnetometry. A biosensor is a device merging biological material and a transducer for detecting cells and diseases. In 2011, (McGuinness et al., 2011) brought the NV center to observe HeLa cells being tissue culture cell line of human. Using position, spin-level and spin coherence specific to locations of HeLa cells. In 2018, (Guarina et al., 2018) studied the effect of fluorescent nanodiamonds (FNDs) in organisms using mouse nervous system or hippocampal neurons since cell culture. As a result, FNDs show action potential in their cells to measure difference while does not affecting nerve cells. In 2020, (Miller et al., 2020) used the NV center as an ultrasensitive label to detect the HIV virus. The virus is annealed between base by primer and FNDs are flowed into the virus. They can detect signals from magnetic resonance with NV center fluorescence. We can bring NV center to measure the magnetic field in matter. In 2014, (Müller et al., 2014) used NMR technique to demonstrate coupling between NV center and silicon with field gradient and achieve high signal-to-noise ratio. In 2015, (DeVience et al., 2015) used NV center to characterize NMR, where fluorinated sample with hydrogen and fluorine compound can be detected via the NV NMR spectra measurement.

These works use NV center to sense changing magnetic field in microscale samples. For our work, the NV center is utilized to do vector magnetometry and mapping unknown magnetic fields with ensemble NV center in macroscale sample, being a magnet.

CHAPTER III

RESEARCH METHODOLOGY

Research methodology presents the Quantum Diamond Spectrometer setup consisting of an optical system and an electronic system. Subsequently, we illustrate signal detection via optically detected magnetic resonance (ODMR) pulse sequences. The pulse sequences involve a microwave generator to sweeping and determine the magnitude and orientation of the magnetic field. Ultimately, we will briefly examine the utilization of magnetic field computations in vector magnetometry and magnetic field mapping.

3.1 Quantum Diamond Spectrometer or QDS

Confocal microscopes are commonly employed in investigations with NV due to their ability to provide high-resolution imaging and to facilitate convenient selection of focusing settings. For instance, confocal microscopes can conduct NV center scanning probes, providing a magnetic field image of 30 nm iron oxide nanoparticles with a spatial resolution of 100 nm (Mosavian et al., 2024). The confocal microscope is also used to study charge conversion of the NV center (Wood et al., 2024). A confocal microscope with an NV center can also be used to study atomic thermometers for biochemical purposes, with a sensitivity of up to 80 mK/Hz. This technique allows researchers to conduct biochemical studies at the femtoliter scale (Li et al., 2024).

However, confocal microscopes take a long time to scan and can hardly track high-speed changes in magnetic fields. Due to rapid changes in capabilities and straightforward optical alignment, we employ the Quantum Diamond Spectrometer (QDS) (Bucher et al., 2019) to achieve high spatial resolution for material characterization. For instance, the QDS offers enhanced fluorescence signals, thereby decreasing data acquisition time and improving spatial resolution for sensor applications. In addition, QDS functions similarly to

nuclear magnetic resonance (NMR) spectroscopy. We use NMR spectroscopy to characterize elements within a substance. In the case of QDS, it is utilized to sense magnetic fields in solid or liquid matter with femtomole sensitivity (Li et al., 2022). The QDS consists of an optical system and an electronic system. The optical system excites electrons in the NV center. The electronic system controls electrons at an energy level transitions.

3.1.1 Optical system

The optical system is used to excite the NV center in Figure 3.1. The system uses a 532 nm green laser as a light source (Coherent OBIS 532 nm). The laser is focused by a convex lens with a focal length of 100 mm (Thorlabs AC254-100-A) to pass through an Acousto-Optic Modulator (AOM) (Gooch & Housego AOMO 3080-120). The AOM creates a diffraction pattern through piezoelectric vibration. The diffracted laser passes to a diaphragm (Thorlabs ID37Z) to create a switch from the diffraction pattern. The first order and zeroth diffraction patterns are defined to be “on” and “off” states. The zeroth-order diffraction pattern is blocked by the diaphragm and the first diffraction pattern passes the diaphragm. The first-order diffraction beam passes through a polarizer and a half-wave plate (HWP). The polarizer and HWP control polarization of the laser before the diamond. The polarized beam is demagnified beam size by beam reducer: a convex lens with a focal length of 200 mm (Thorlabs AC254-200-A) and a convex lens with a focal length of 30 mm (Thorlabs AC254-030-A). The laser is flipped upward to the diamond on the light guide (Edmund optics stock number 49-402) and is focused by a convex lens with a focal length of 50 mm (Thorlabs AC254-050-A). The focused laser passes through the light guide to the diamond and goes out from the other side due to total internal reflection. The red fluorescence from the diamond goes through the light guide to the avalanche photodetector (APD) (Laser components A-CUBE-S3000-03). The APD places two filters before the detector, one to block the green laser (Thorlabs NF533-17) and the other to select the desired wavelength (Thorlabs FELH0600). Then, the APD signal is sampled by

NI-DAQ (National Instruments PCIe-6363) and sent to the computer for processing and calculating data.

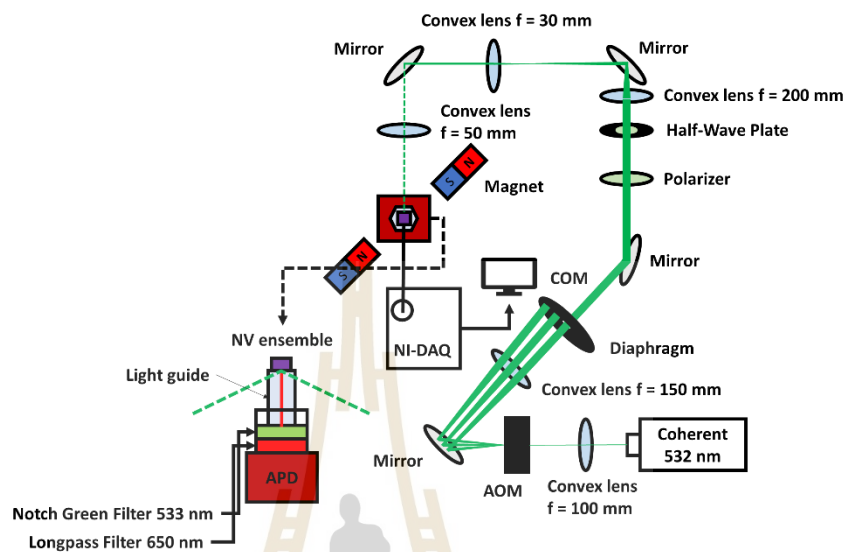


Figure 3.1 Quantum Diamond Spectrometer (QDS) schematic.

3.1.2 Electronics system

The electronics system controls RF output from the signal generator to the microwave loop to manipulate the electron spin states of the NV center, as shown in Figure 3.2. The signal is generated by a microwave source (RIGOL DSG836) and sent to a microwave switch (Mini-circuits ZASWA-2-50DRA+). The switch controls the RF signal to the microwave loop by a transistor-transistor logic (TTL) signal from PulseBlaster (PulseBlaster ESR-Pro-500). The switch has 2 output ports consisting of OUT1, the first port, and OUT2, the second port. When the TTL signal is in a high state, radio frequency (RF) impulses are received through the RF-IN port and subsequently transmitted over the OUT2 channel. Another output port, denoted as OUT1, is terminated with a 50-ohm impedance (Mini-circuits ANNE-50+) to prevent the generation of reflected signals. The signals in the OUT2 channel undergo a high-pass filter (Mini-Circuits VHF-1600+) for noise filtering and are amplified by an amplifier (Mini-Circuits ZHL-16W-43-S+). An attenuator (Mini-Circuits VAT-10A+) is added before the amplifier to protect the amplifier from damage. The amplified

signal is driven to a circulator (Ditom D3C2040) before reaching the microwave loop to protect the amplifier from potential harm, while the reflected signal on the circulator is ended by a terminator. Finally, the microwave loop sends signals to the diamond.

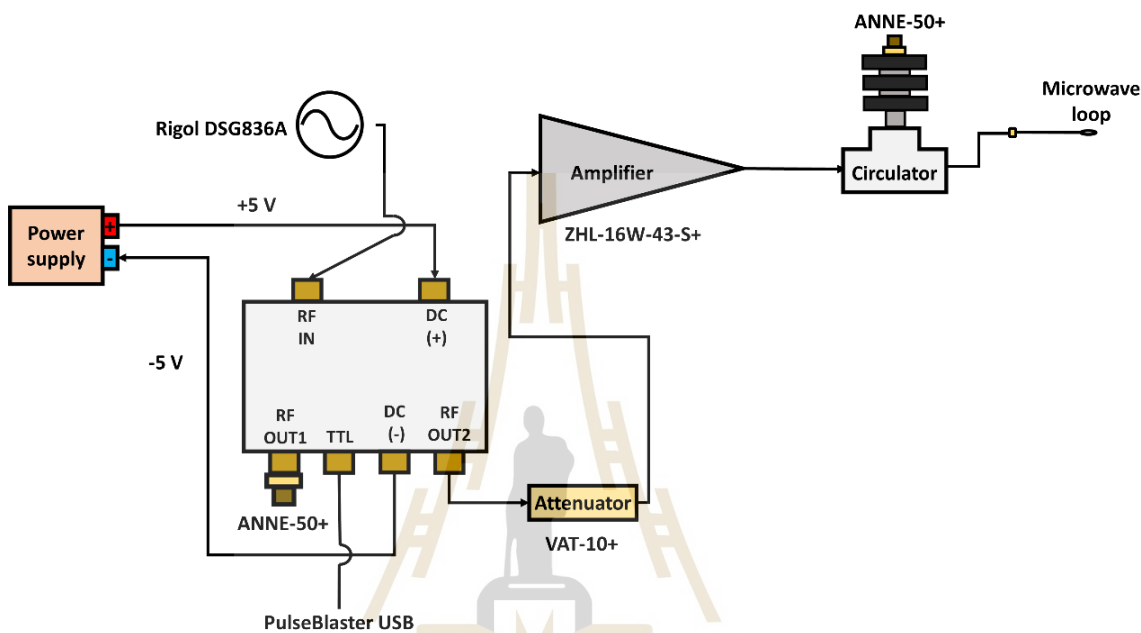


Figure 3.2 Electronic diagram for controlling microwave.

3.2 Pulse sequence

Electrons are controlled to occupy the desired energy level with pulse sequences. The pulse sequence creates each pulse with each duration for specific instruments. As a result, pulse duration relates to manipulating electrons in experiments.

3.2.1 Optically Detected Magnetic Resonance (ODMR)

Optically Detected Magnetic Resonance (ODMR) is an integration of electron spin resonance (ESR) and optical measurements. ODMR can represent the relation between optical measurement and microwave frequency. The ODMR pulse sequence uses 3 components: a 532-nm laser (“Green”), microwave (“MW”), and avalanche photodetector (“APD”) in figure 2.5. The ODMR pulse sequence consists of 2 sequences, continuous wave

(CW) ODMR and pulsed ODMR. CW ODMR is a measurement technique releasing continuous microwave and laser. In the figure 2.5A, we start with “Green” turning the laser on and “MW” turning the microwave on. Following that, there is waiting time to turn on “APD” for detection. In the end, it will go back to the initial point and continue the loop with “n” rounds. For the second loop, it is reference detection due to no “MW”. Pulsed ODMR is a rhythmic signal transmission in figure 2.5B. The pulse sequence begins with "Green" turning on the laser for the "Initialization time" for NV polarization. In this process, electrons at a mixed state are polarized to $m_s = 0$ for state preparation. After that, the laser is turned off to repolarize the condition during "relaxation time". After that, the microwave is turned on to excite electrons from $m_s = 0$ to $m_s = 1$ throughout the "Microwave time" duration. After that, "APD" detects signals within the detection range of "Pulsewidth". At the end of green, it will return to the beginning and repeat the loop with "n" rounds. The first loop detects signals. Because there is no microwave, the second loop detects reference signals. We combine data from signal and reference detection to split it for photoluminescence.

The difference between CW ODMR and pulsed ODMR is pulse. CW ODMR releases microwave and laser continuously. The continuous release makes a wider linewidth due to laser repumping and microwave broadening over the whole experiment, which leads to low sensitivity (Levine et al., 2019). The effect is reduced by employing lock-in detection with strong laser and microwave intensity instead (Barry et al., 2020). Pulsed ODMR, on the other hand, uses appropriate duration for laser initialization, microwave manipulation, and readout to reduce repumping and power broadening effects. Separation makes electrons repolarize the state efficiently for the next initialization causing a linewidth reduction (Levine et al., 2019). The narrow linewidth indicates higher sensitivity because it distinguishes splitting correctly. In addition, the pulse duration for operating the pulsed ODMR experiment relating to pulsed ODMR in Figure 3.3 is in table 2.1.

After adjusting pulse duration and establishing setup, we find the resolution of setup through ODMR sequence. The resolution is the full-width half maximum (FWHM) of

a dip in Zeeman splitting. In this case, the first dip is used to find the FWHM. So, the resolution is 26 MHz in figure 3.4.

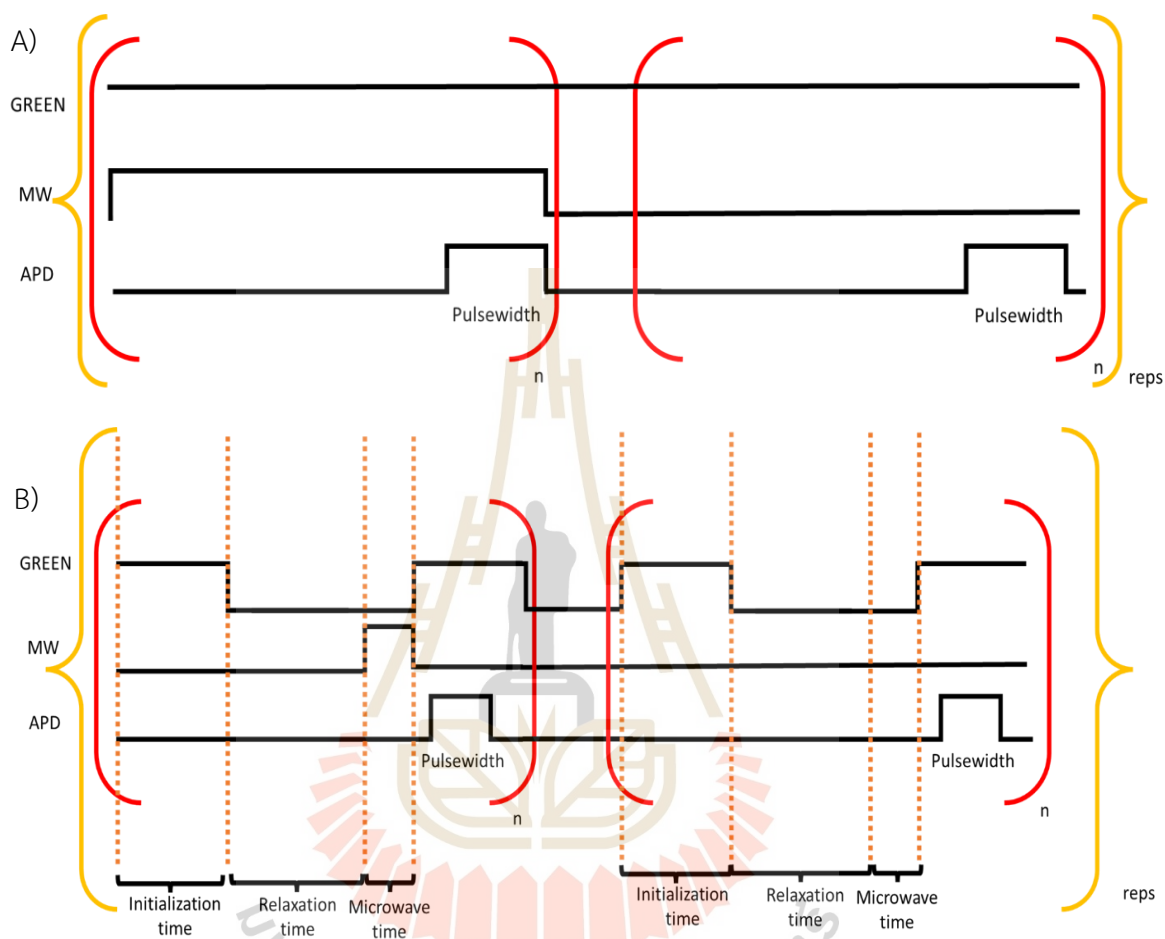


Figure 3.3 ODMR sequence is designed to find the position of an energy level of a NV for control sequence. Figure A) is Continuous Wave (CW) ODMR. Figure B) is pulsed ODMR.

Table 2.1 Pulse duration for Pulsed ODMR.

Name	Duration
Initialization time	3 – 5 microseconds
Relaxation	1 – 5 microseconds
MW time	0.05 – 1 microseconds
Pulsewidth	-

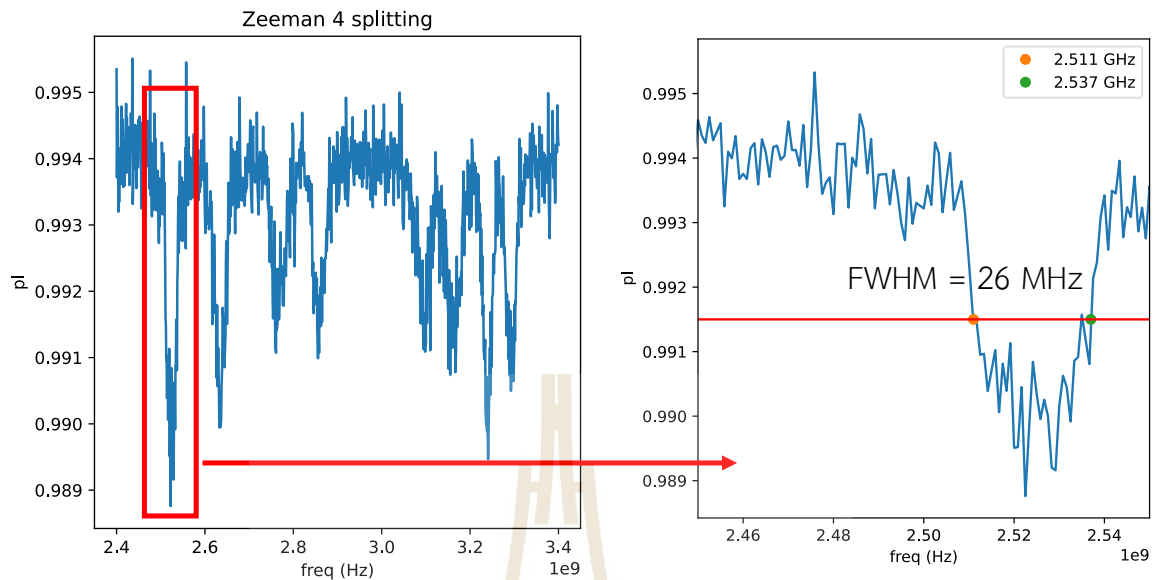


Figure 3.4 The full width half maximum (FWHM) of system is 26 MHz with using the first dip of Zeeman 4 splitting.

3.3 Microwave generator

To manipulate electrons in the NV center, radio-frequency (RF) signals are required to excite electrons from the ground state. These RF signals are generated by a microwave generator (Rigol DSG836), which offers a tunable power range from -100 dBm to +20 dBm, a maximum frequency of 3.6 GHz, and a frequency resolution of 0.01 Hz.

This thesis aims to demonstrate high-speed vector magnetometry. The microwave source supports real-time or near real-time signal generation via its frequency-sweeping function, capable of transmitting RF signals at intervals of 50 ms per frequency step.

3.4 Determining magnetic field magnitudes and orientations

The determination focuses on the detecting signal process and automation program development. Following that, the magnetic field magnitude and orientation calculation are presented.

3.4.1 Signal detection process

The fluorescence signal from the diamond is continuously emitted and directed to the detector. Accurate detection of this signal is achieved using an ODMR pulse sequence, which requires precise timing of control pulses.

A Pulse Blaster is employed to generate these control pulses and to synchronize the operation of four key instruments: the Acousto-Optic Modulator (AOM), an RF switch, a Data Acquisition (DAQ) system, and a microwave (MW) source. The Pulse Blaster sends signals through four output ports:

- The first port (PB0) triggers the AOM to produce a diffraction pattern that modulates the optical path.
- The second port (PB1) activates the RF switch, allowing RF signals from the MW source to pass through.
- The third port triggers (PB2) the DAQ system to record fluorescence data during the pulse sequence. In this experiment, data is collected with a single trigger per sequence, rather than over a periodic interval.
- Finally, the fourth port (PB3) initiates the frequency sweep of the MW source, enabling controlled release of microwave signals.

3.4.2 Program

The program in Figure 3.3 is designed by Qt designer software. The software uses to designing and building graphical user interfaces and is outlined by the microwave generator interface of sweeping program. The program consists of 3 functions: Sweep function, Sweep parameter, and ODMR parameters for setting before starting the experiment.

3.4.2.1 Sweeping function

The sweeping functions in this box are commands that set the microwave source, preparing the system before releasing the signal and waiting for the trigger signal from the external pulse.

3.4.2.2 Sweeping parameters

In this box, the sweeping parameters contain free parameters to adjust sweeping range, such as setting initial and stop frequency for sweeping frequency, microwave power range with setting initial and stop microwave power for sweeping levels, the number of microwave frequencies per sweeping, and the shape of the sweeping signal.

3.4.2.3 ODMR parameters

The ODMR parameters in this box set the pulse duration, including initialization time, relaxation time, microwave time, number of samples, and repetition.

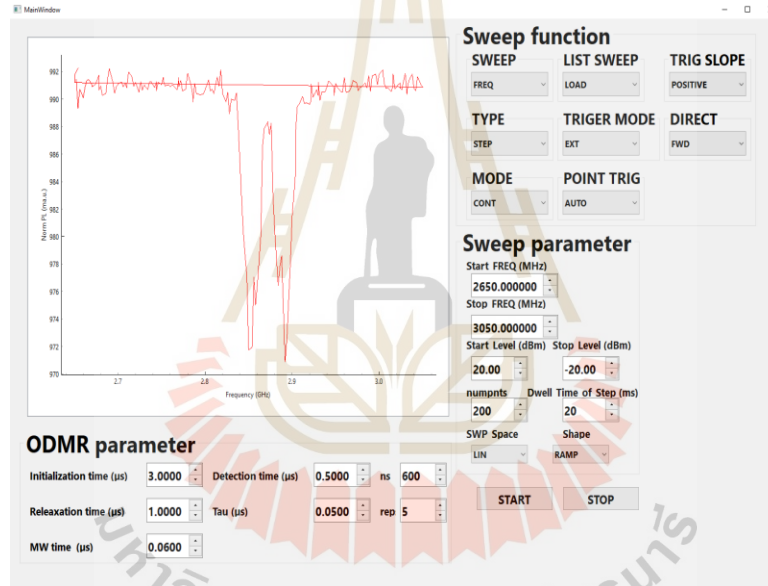


Figure 3.5 The Sweeping program is designed by Qt designer. The program has three main parts “Sweep function”, “Sweep parameter” and “ODMR parameter”.

3.4.3 Magnetic field calculation

The magnitude and direction of a magnetic field can be extracted from the ODMR signal by analyzing its frequency splitting behavior. In this system, the external magnetic field interacts with the NV centers in diamond, specifically affecting the spin states of electrons. This interaction leads to a characteristic splitting in the ODMR spectrum, which can be used to determine both the field magnitude and its spatial orientation.

For simplicity, the interaction is first illustrated with respect to a single NV axis, as shown in Figure 3.4. The external magnetic field \mathbf{B} forms an angle α with this NV axis. The magnetic field causes a Zeeman splitting of the energy levels, resulting in two resonant frequencies in the ODMR signal. Using this splitting, the magnetic field's magnitude and orientation can be derived from Eq. 3 and Eq. 4 originated from eigenvalues of NV Hamiltonian.

Eq. 3 calculates the magnetic field magnitude, while Eq. 4 determines the field orientation. These expressions are derived from the eigenvalue solutions of the NV center's spin Hamiltonian. The magnitude B is calculated based on the frequency difference between the two ODMR peaks (ω_1 and ω_2), the zero-field splitting constant D , and the NV center's gyromagnetic ratio γ_{NV} . The angle α represents the angle between the NV axis and the magnetic field direction.

The calculated magnetic field magnitude represents the component of the field acting along a single NV axis. Since the NV center has four crystallographic orientations, the full magnetic field vector can be reconstructed by averaging the results from all four axes. This provides a more comprehensive representation of the magnetic field acting on the NV center

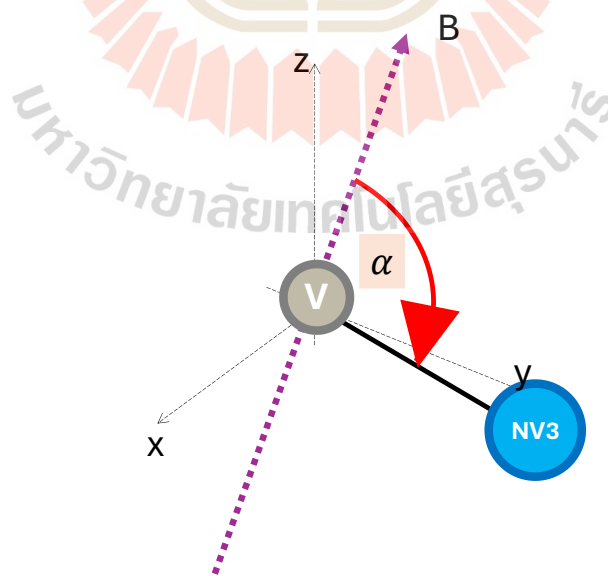


Figure 3.6 An NV axis and magnetic field in the system. The angle between the magnetic field and an NV axis is called alpha and is calculated by Eq. 4.

$$B = \frac{\sqrt{(w_1^2 + w_2^2 - w_1 w_2 - D^2)/3}}{\gamma_{NV}}, \quad \text{Eq. 3}$$

$$\alpha = \arccos \left(\pm \sqrt{\frac{(2w_1 - w_2 - D)(w_1 - 2w_2 + D)(w_1 + w_2 + D)}{[9D(w_1^2 - w_1 w_2 + w_2^2 - D^2)]}} \right). \quad \text{Eq. 4}$$

While the direction of the magnetic field is inferred through the angular relationship α with respect to the NV axis, it does not uniquely determine systematic magnetic field direction. So, the set of all vectors forming the same angle α with an NV axis defines a cone surface, and thus the possible magnetic field directions lie on this conical surface. Due to vector symmetry, both positive and negative field directions result in two cones per NV axis.

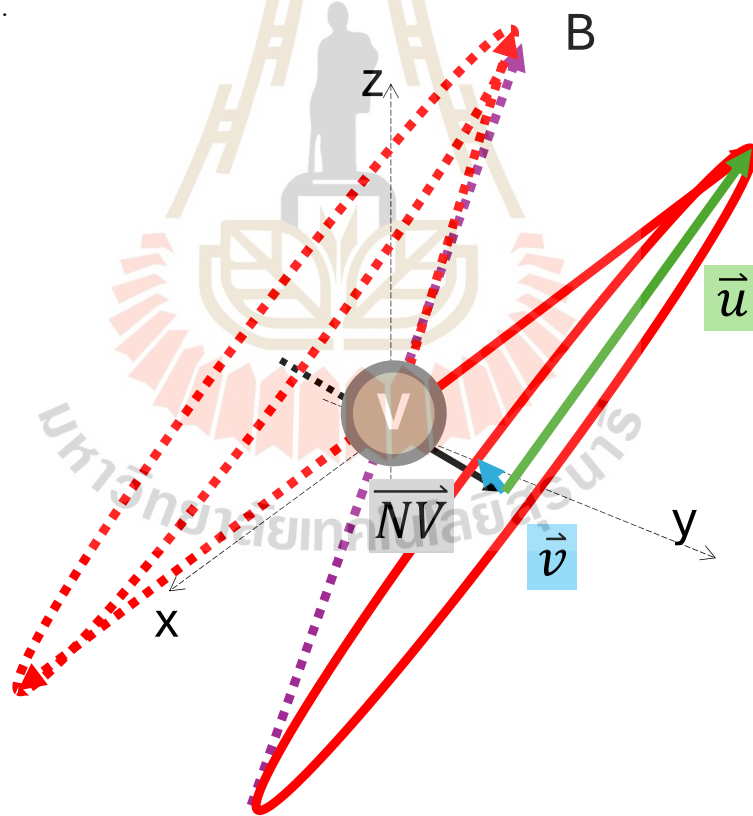


Figure 3.7 The two cones represent possible magnetic field directions to act on an NV axis. The cone surface is described mathematically by orthogonal vector between \vec{u} (blue vector) and \vec{v} (green vector) constraining both vectors are perpendicular with the NV axis or \vec{NV} (black vector) and each other.

To mathematically describe this surface like Figure 3.5, two orthogonal \vec{u} and \vec{v} are introduced. These vectors are perpendicular to the NV axis and to each other, forming a local coordinate system for the cone. \vec{u} is obtained by solving the dot product in Eq. 5.

$$\overline{NV} \cdot \vec{u} = 0 \quad \text{Eq. 5}$$

$$\overline{NV} = [NV_x, NV_y, NV_z], \quad \text{Eq. 6}$$

$$\vec{u} = [u_x, u_y, u_z]$$

$$\text{So, } 0 = [NV_x, NV_y, NV_z] \cdot [u_x, u_y, u_z] \quad \text{Eq. 7}$$

$$\text{From Eq. 5, } 0 = NV_x u_x + NV_y u_y + NV_z u_z \quad \text{Eq. 8}$$

$$\text{From Eq. 6, if } u_z = 0, \quad u_x = -NV_y \text{ and } u_y = NV_x \quad \text{Eq. 9}$$

$$\therefore \vec{u} = [u_x, u_y, u_z] = [-NV_y, NV_x, 0]$$

This condition ensures orthogonality. Multiple solutions can satisfy this condition, but for simplicity, the component u_z is set to zero. This leads to the explicit form of \vec{u} in Eq. 9. The second orthogonal \vec{v} is obtained via the cross product of \overline{NV} and \vec{u} , as given in Eq. 10. The resulting \vec{v} is normalized in Eq. 11, ensuring unit length for consistent directional analysis. Finally, both \vec{u} and \vec{v} are normalized to form a basis for constructing direction vectors on the cone's surface, as shown in Eq. 12.

$$\vec{v} = \vec{u} \times \overline{NV} \quad \text{Eq. 10}$$

$$\vec{v} = [-NV_y, NV_x, 0] \times [NV_x, NV_y, NV_z] \quad \text{Eq. 11}$$

$$\therefore \vec{v} = [NV_x NV_z, NV_y NV_z, -NV_x^2 - NV_y^2]$$

$$\therefore \hat{u} = \frac{[-NV_y, NV_x, 0]}{\sqrt{(-NV_y)^2 + NV_x^2 + 0^2}},$$

$$\hat{v} = \frac{[NV_x NV_z, NV_y NV_z, -NV_x^2 - NV_y^2]}{\sqrt{(NV_x NV_z)^2 + (NV_y NV_z)^2 + (-NV_x^2 - NV_y^2)^2}} \quad \text{Eq. 12}$$

A special set of vectors on the cone surface, whose component on the NV axis is constrained to 1, representing a possible magnetic field direction, is then expressed as:

$$\therefore \widehat{NV} + (\hat{u} \sin t + \hat{v} \cos t) \tan \alpha = [x, y, z] \quad \text{Eq. 13}$$

where t is a free parameter sweeping from $-\pi$ to π on the cone plane. The result is a set of magnetic field direction vectors in Cartesian coordinates relative to the NV frame. These coordinates are then transformed into the laboratory frame and can be converted into spherical coordinates using trigonometric relationships. The resulting angles— θ (inclination) and ϕ (azimuth)—are given in Eq. 14 and 15.

$$\theta = \cos^{-1} \frac{z}{\sqrt{x^2 + y^2 + z^2}} \quad \text{Eq. 14}$$

$$\phi = \tan^{-1} \frac{y}{x} \quad \text{Eq. 15}$$

Each NV axis produces two possible directional curves (positive and negative cones) in spherical coordinates. These solution sets can be visualized as lines on a spherical surface, as shown in Figure 3.6. Consequently, a single NV axis provides two possible cones of magnetic field solutions.

In a typical NV center, there are four different crystallographic orientations. Each orientation yields its own pair of solution cones in Figure 3.7. When all four solution sets are combined, their intersections correspond to the actual direction of the magnetic field. This intersection analysis is illustrated in Figure 3.8. By identifying the common intersection among the four solution sets, both the orientation and magnitude of the external magnetic field acting on the NV center can be accurately determined.

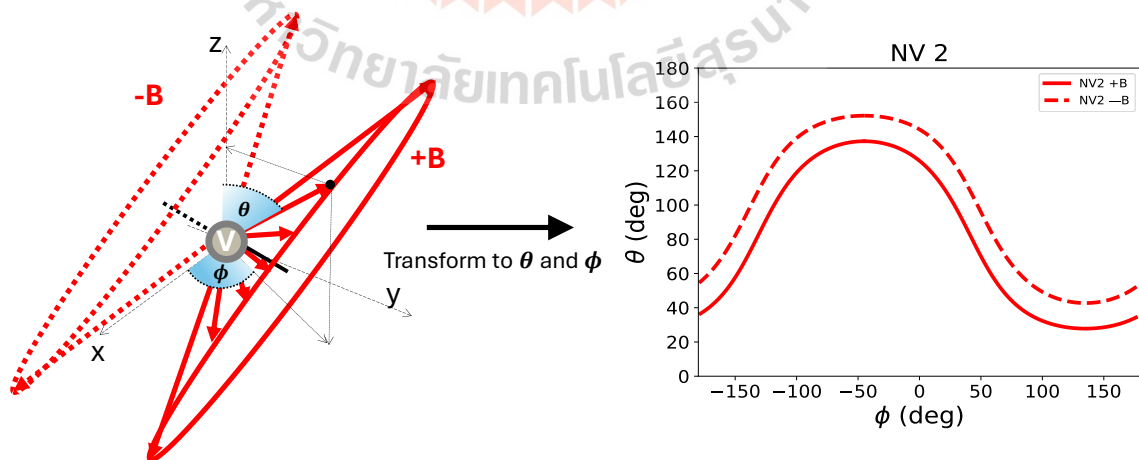


Figure 3.8 Transformation from Cartesian coordinate to spherical coordinate using trigonometry. The answer set in the graph represents positive and negative magnetic field orientation possibilities that act on the NV axis.

3.4.4 Experimental workflow

The section presents experiments that validate the setup's ability to detect signals accurately and the precision of the magnetic field calculations in determining orientation and magnitude. First, the QDS detects signals from ODMR. The ODMR signal is then analyzed through simulation to examine NV excitation. Next, the magnetic field calculation is tested using simulations, raw ODMR data, and specific test cases. Finally, the magnetic field calculation is integrated with QDS to perform vector magnetometry, demonstrating both the orientation and magnitude of the magnetic field.

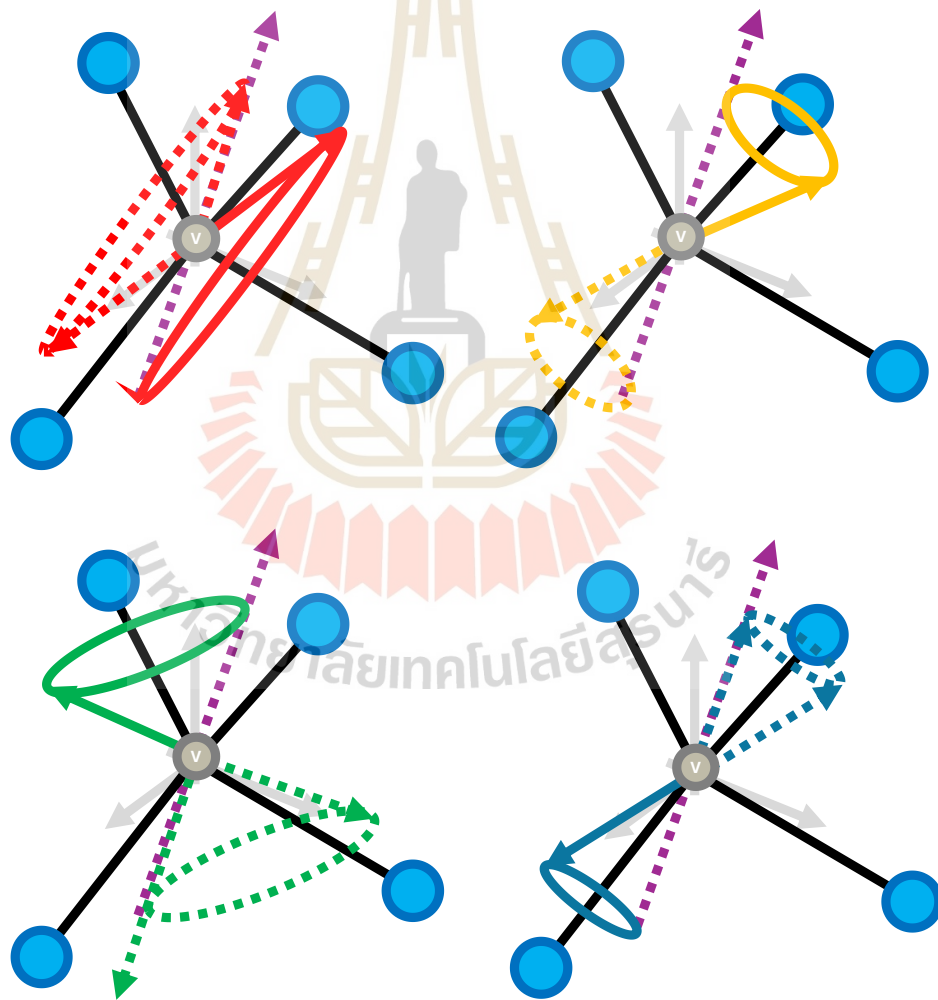


Figure 3.9 The 4 orientations of the NV center senses magnetic field in the specific direction and create cones along NV axes.

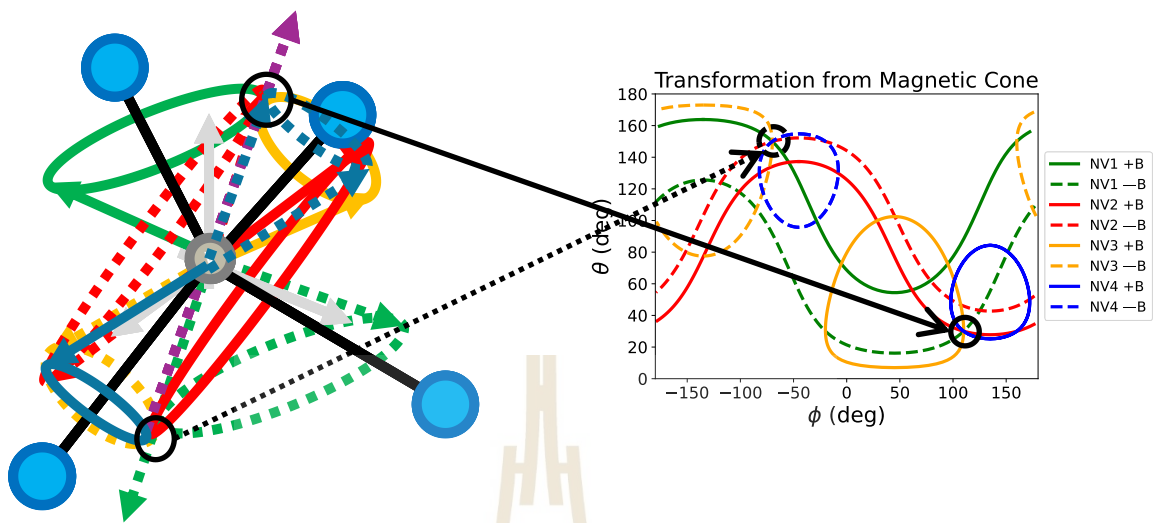


Figure 3.10 3D and 2D graphs represent that answer sets of 4 NV axes are not unique and have interceptions. The interceptions show real magnetic field direction acting on the NV center in positive and negative field.

CHAPTER IV

RESULT AND DISCUSSION

Chapter IV will discuss and analyze the experimental results from the testing magnetic field calculations with various cases, such as Reference measurement and Special cases. Moreover, using NV center allows unknown magnetic field mapping from ODMR signals.

4.1 Validation measurements

Prior to measurement, the setup is validated by observing all Zeeman-effect-induced splitting cases, ranging from one to four splittings in the ODMR signal. These splittings reflect the orientation of the applied magnetic field relative to the four crystallographic axes of the NV centers. When the magnetic field is oriented perpendicular to an NV axis, the ODMR spectrum exhibits a single splitting. This indicates that all four NV orientations experience the magnetic field with the same magnitude and direction.

In contrast, when the magnetic field is not perpendicular to the NV axes, the ODMR signal displays between two and four splitting. A four-splitting scenario implies that each NV axis senses the magnetic field with a distinct direction and magnitude. In the case of two or three splitting, this suggests that certain NV axes are exposed to identical magnetic field vectors, resulting in overlapping resonance frequencies. Thus, some splitting may represent multiple NV orientations.

To establish a reference dataset, measurements are conducted under controlled magnetic field orientations to produce each type of splitting. Specifically, a single splitting is achieved with $\theta = 90^\circ$ and $\phi = 0^\circ$, two splitting with $\theta = 80^\circ$ and $\phi = 0^\circ$, three splitting with $\theta = 80^\circ$ and $\phi = -10^\circ$, and four splitting with $\theta = 70^\circ$ and $\phi = -10^\circ$. These reference signals serve as benchmarks for later magnetic field analysis.

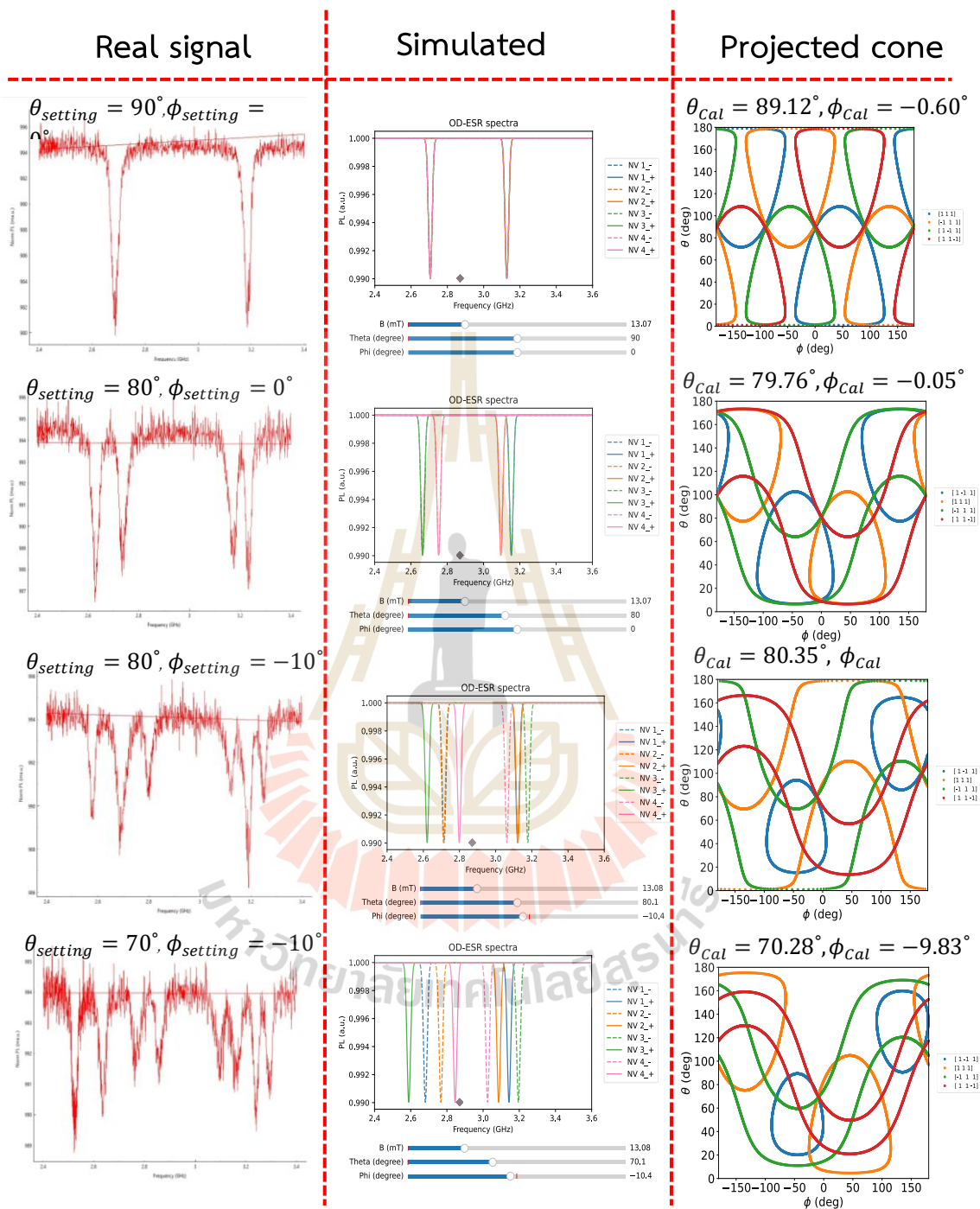


Figure 4.1 Result from magnetic field calculation represents comparison between real signal, simulated signal and projected cone. The Real signal is the detected ODMR signal. The simulated signal from the simulation program is to match NV axes and ODMR splitting. The projected cone is the calculated results.

Magnetic field calculations are based on these reference data to determine both field magnitude and orientation. Accurate determination of the NV axes associated with each splitting is necessary and is achieved using a simulation program based on the Hamiltonian of the NV center. The program allows adjustment of the magnetic field strength (B), polar angle (θ), and azimuthal angle (ϕ) to produce a simulated ODMR spectrum that closely matches the measured reference data. This process ensures that the simulated signals reflect the actual NV axis orientations.

For consistency, each reference splitting case must correspond to the same calculated magnetic field magnitude. The resulting field magnitudes are closely aligned, with values of 153.05 G, 162.55 G, 157.10 G, and 167.84 G for one to four splitting cases, respectively. Magnetic field orientation is then determined from the reference data using the simulation-based calculation, and the resulting vector orientations are validated through graphical analysis of their intersections. This confirms the accuracy and reliability of the magnetic field method in Figure 4.1.

4.2 Resolution test

This topic proves that magnetic field calculations can distinguish similar ODMR signals of different magnetic field orientations, and ODMR signals from small angle changes.

4.2.1 Magnetic field from different directions with similar ODMR signal

In this case, although the magnetic field orientation angles differ, both configurations produce observable ODMR signals. The red ODMR signal corresponds to a magnetic field orientation of $\theta = 150^\circ$ and $\phi = 50^\circ$, while the blue ODMR signal corresponds to $\theta = 160^\circ$ and $\phi = 70^\circ$. The ODMR spectra exhibit similar overall profiles, with some splitting occurring at identical frequency positions. However, a notable difference is observed in the third splitting of the blue ODMR signal, which shifts closer to the second splitting of the red signal with black arrows in Figure 4.2.

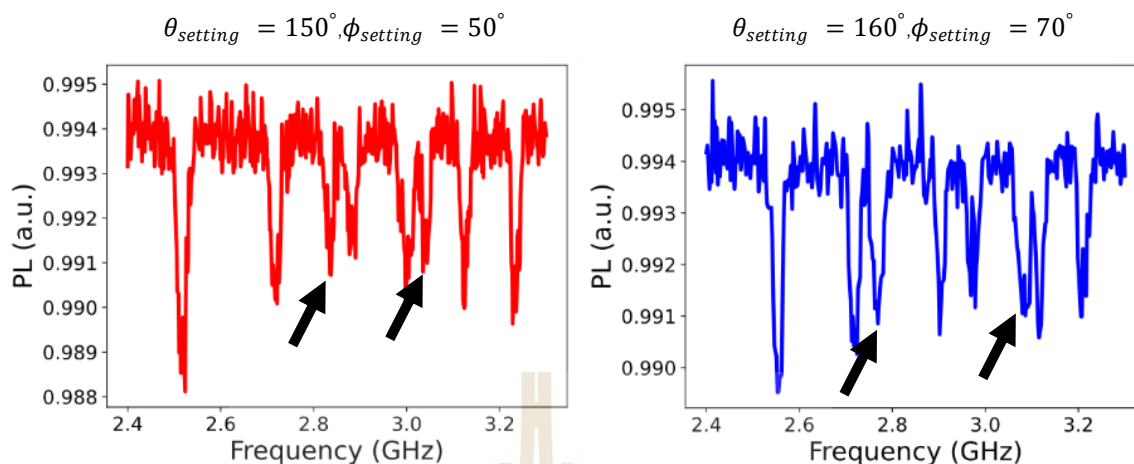


Figure 4.2 Two ODMR signals with similar shape acquired when θ and ϕ is set to 150° , 50° (red), and 160° , 70° (blue). The third splitting of red ODMR is shift close to second splitting in the blue ODMR following the black arrow.

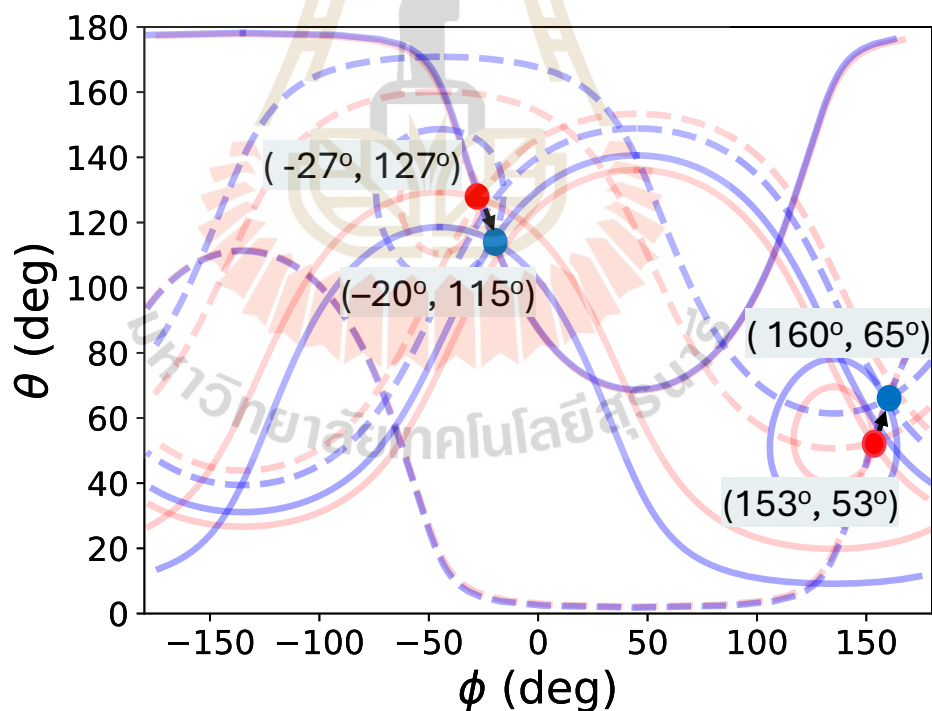


Figure 4.3 the calculation result of the first special case. The blue and red curves are the calculated results of NV axes that sense magnetic field from the blue and red ODMR signal respectively. The interceptions of blue and red curves are orientation of magnetic field.

To analyze this phenomenon, magnetic field orientation is determined through computational reconstruction. The calculated results yield solution sets for both ODMR signals in spherical coordinates. In the corresponding graphical representation, the red and blue curves represent the solution sets for the respective magnetic field configurations. Blue curves intersect at $\theta = 160^\circ$ and $\phi = 65^\circ$. Red curves intersect at $\theta = 153^\circ$ and $\phi = 53^\circ$. Notably, the intersection points for the red and blue curves do not coincide with each other in Figure 4.3

In Figure 4.3, certain segments of the red and blue curves overlap, indicating that some NV axes perceive identical magnetic field directions and magnitudes. Conversely, the non-overlapping portions suggest that other NV axes experience different magnetic field vectors. This demonstrates that NV centers are capable of detecting changes in both the direction and magnitude of the magnetic field.

4.2.2 ODMR signal with small angle differences

This section examines the system's ability to resolve small angular differences in magnetic field orientation by varying one angle while keeping the other constant. Two subcases are considered: (1) varying the polar angle θ while holding the azimuthal angle ϕ constant, and (2) varying ϕ while keeping θ fixed. Each subcase is evaluated through magnetic field reconstruction based on the corresponding ODMR signals.

In the first subcase, θ is varied slightly while ϕ is fixed at 165° . The red ODMR signal corresponds to $\theta = 68^\circ$, and the blue signal to $\theta = 70^\circ$. The computed results yield solution sets represented by red and blue curves in spherical coordinate space. At first glance, these curves appear to intersect at the same point. However, upon closer inspection of the small graph, the intersection points differ slightly, and the calculated angles are closely aligned with the actual input values. This indicates that the magnetic field calculation accurately resolves small variations of θ in Figure 4.4. In addition, if the curves do not intercept, we average the center area for defining interception.

In the second subcase, ϕ is varied while θ is fixed at 70° . The red ODMR signal corresponds to $\phi = 157^\circ$, and the blue signal to $\phi = 155^\circ$. Similar to the first case, the

resulting solution sets appear to overlap, but a magnified view of the graph reveals distinct intersection points. Again, the reconstructed angles closely match the original settings. These results in Figure 4.5 demonstrate that the magnetic field reconstruction method can effectively distinguish between similar ODMR spectra corresponding to nearby magnetic field orientations. The method is sensitive to subtle changes in both polar and azimuthal angles, highlighting its robustness and precision.

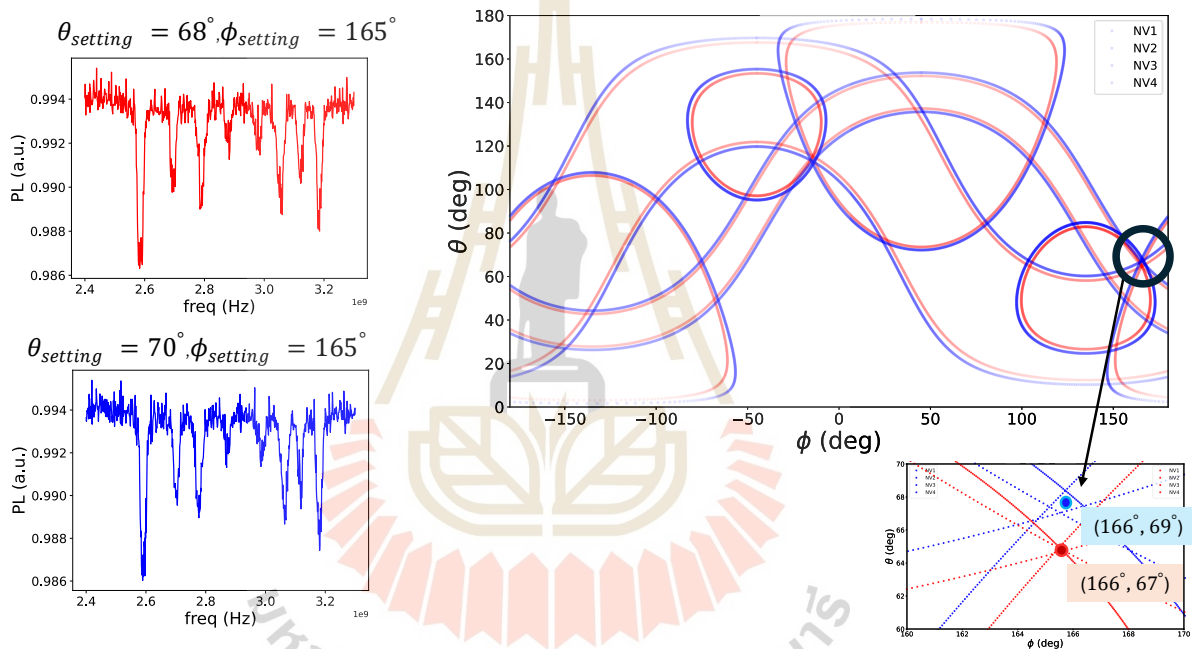


Figure 4.4 the two ODMR signals with small difference acquired when θ and ϕ is set to 68° , 156° (red), and 70° , 165° (blue). The blue and red curves are the calculated result of NV axes. The calculated result present that the calculation distinguishes the small difference in the small figure when calculated θ and ϕ is 69° , 166° (red dot), and 67° , 166° (blue dot).

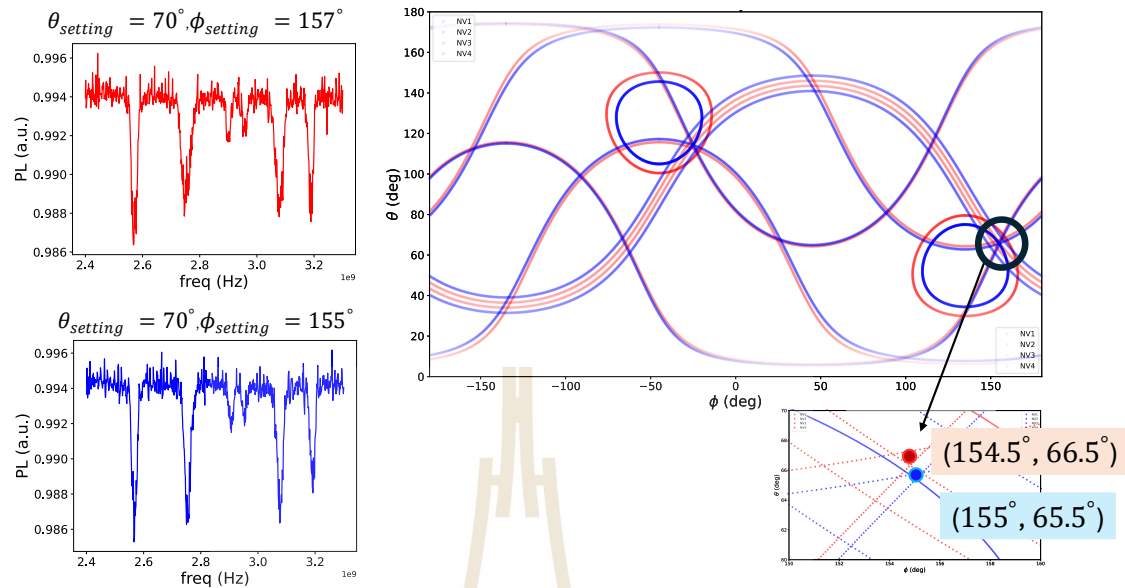


Figure 4.5 the two ODMR signals with small differences acquired when θ and ϕ is set to 70° , 157° (red), and 70° , 155° (blue). The blue and red curves are the calculated results of NV axes that sense difference in from the blue and red ODMR signal respectively. The calculated result present that the calculation distinguishes the small difference in the small figure when calculated θ and ϕ is 66.5° , 154.5° (red dot), and 65.5° , 155° (blue dot).

4.3 NV center as a magnetic field scanner

Previously, we demonstrated vector magnetometry with ensemble NV center. IN this case, the NV center is going to be used as a sensor to image \vec{B} from permanent magnet in the north pole direction in the new perspective.

Typically, when measuring the magnetic field at a specific location, a magnetic field sensor is placed directly at that position to detect both the field's magnitude and direction. In Figure 4.6, the black box with arrows indicating the magnetic field direction represents the magnetic field sensor, while the gray box denotes the magnet. When the sensor is positioned on the left side, it detects a magnetic field oriented in a southwest direction. As the sensor is moved toward the center of the region, the detected direction gradually shifts to the North Pole. At the system's center, the field direction points directly to the North Pole. Moving the sensor to the right-side results in a continued change in direction,

now pointing southeast direction. Notably, the magnetic field direction at the right side is approximately opposite to that on the left. This configuration is referred to as the **"scanning-NV perspective"**, wherein the NV center functions as a fixed sensor scanning the magnetic field.

In our experimental setup, however, the NV center cannot be moved due to physical constraints. To demonstrate vector magnetometry using NV centers under these conditions, the magnet itself is moved instead. This approach is termed the **"moving-magnet perspective"**. Figure 4.7 illustrates a comparison between these two perspectives: panels a), b), and c) show the moving-magnet perspective, while panels d), e), and f) depict the corresponding scanning-NV perspective. For example, in the moving-magnet configuration, when the magnet is placed at position A, the sensor detects a field pointing. In the corresponding scanning-NV view, this same field orientation appears reversed due to the frame of reference. When the magnet is positioned at the center (position B), the moving-magnet perspective detects a field pointing outward, while the scanning-NV perspective again shows an opposing direction. Similarly, at position C, the detected field direction in the moving-magnet setup is opposite to that at position A, while in the scanning-NV configuration, it remains consistent in its reversed relation.

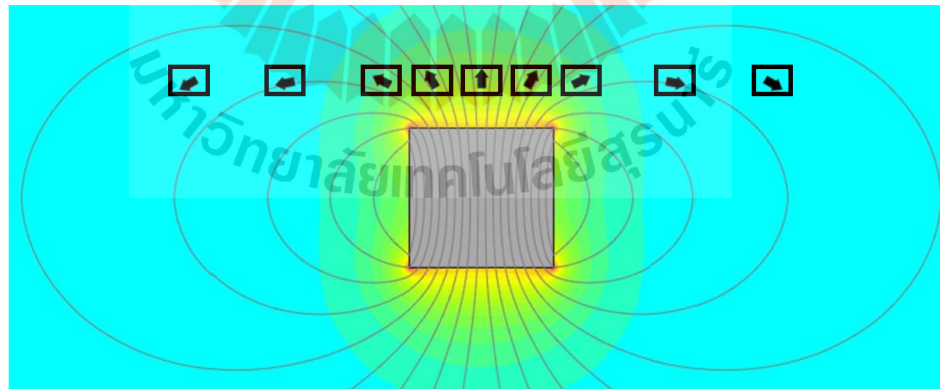


Figure 4.6 The magnetic field in scanning-NV perspective is observed by sensor. When the magnetic field sensor is moved gradually from the left position to the center position, the magnetic field direction is changed from the left direction to pointing out of the magnet. Moving sensor from the center magnet to the left positions is changed direction from pointing out to right direction.

Consequently, all experimental results are reported in the scanning-NV perspective, with interpretations flipped from the moving-magnet reference frame. Furthermore, the experiment is designed to observe the magnetic field near the north pole of the magnet, where the field diverges outward from the magnet's center, and the magnitude decreases with increasing distance from the center.

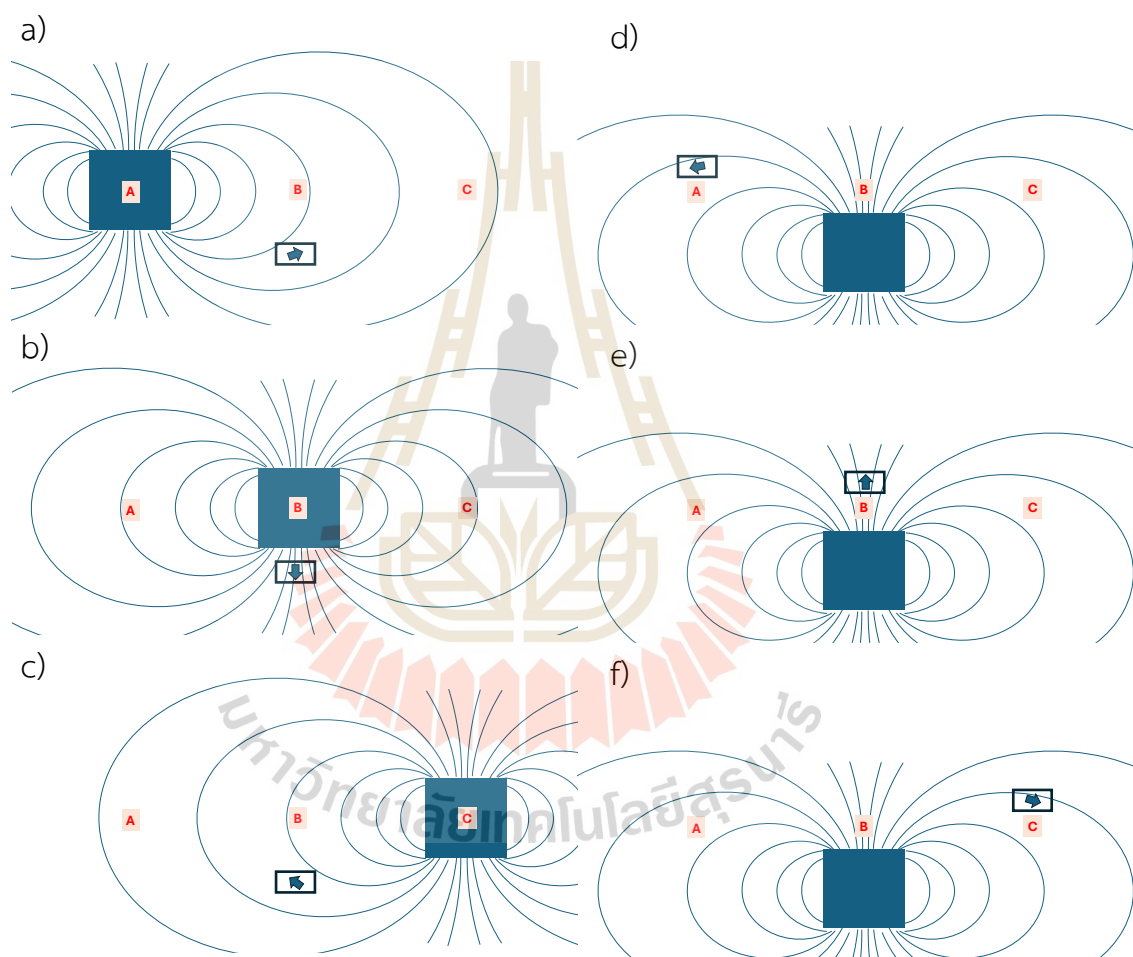


Figure 4.7 The picture a), b), c) represent magnet is moved at the different position and NV center sense different magnetic field direction as a position in moving-magnet perspective. The picture d), e), f) pictures represent the corresponding scanning-NV perspective of a), b), c) respectively. When NV is a small box with arrow indicating the magnetic field direction, and magnet is blue box.

4.4 Setup for magnetometry

Due to the constraints of the experimental setup, the magnet is moved instead of the sensor. To facilitate this, the dial component of the setup was removed, and a flat plate was positioned approximately 1.7 cm above the NV center. A sheet of graph paper was affixed to the plate to define a coordinate system for the magnet's movement in the x and y directions, as illustrated in Figure 4.8. During the experiment, the ODMR signal was measured as a function of the magnet's position across 5 x 5 cm detection area (see Figure 4.9). The collected data were organized into a two-dimensional array corresponding to spatial positions. Each data point was then processed using a magnetic field reconstruction algorithm to determine the local magnetic field magnitude and orientation. Finally, the results of the calculation were used to extract the magnetic field components in the x, y, and z directions at each measurement position.

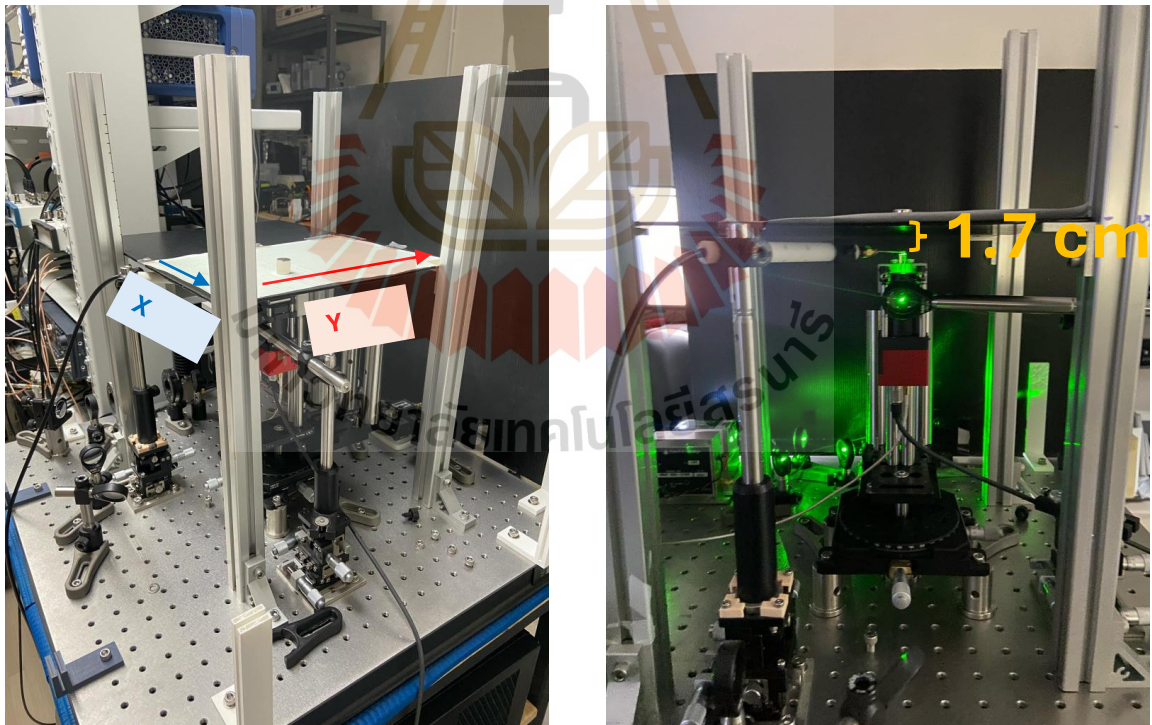


Figure 4.8 The new setup without magnet on dial has a plate for moving magnet plane with magnet on the top of plate. The distance between magnet and NV center on the top of lightguide is 1.7 cm.

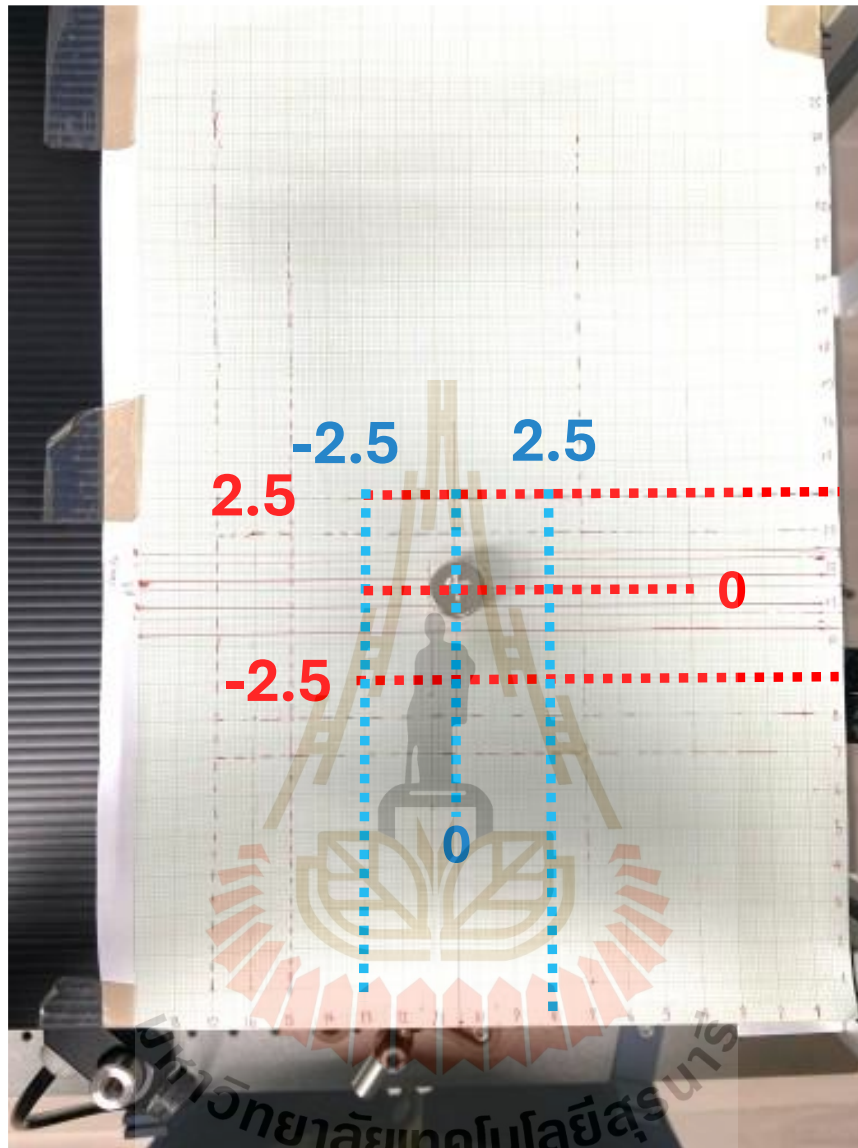


Figure 4.9 The plate is attached by graph paper. The graph shows detection area for experiment with setting the center of the system at 0 and border from 2.5 to -2.5 in x and y direction.

4.5 Magnetic field strength above the NV center at 1.7 cm

In vector magnetometry, the results—presented from the scanning-NV perspective—include the total magnetic field magnitude B_{total} , as well as the individual

magnetic field components along the z-axis (B_z), x-axis (B_x), and y-axis (B_y), all plotted on the same spatial scale in the xy plane in Figure 4.10.

The B_{total} illustrates the spatial distribution of field strength across the xy plane. At the center of the detection area, the magnitude reaches its maximum value due to the proximity of the magnet to the NV center. As the magnet is moved away from the center, the field strength decreases gradually, with more significant attenuation observed at the outer edges of the detection region.

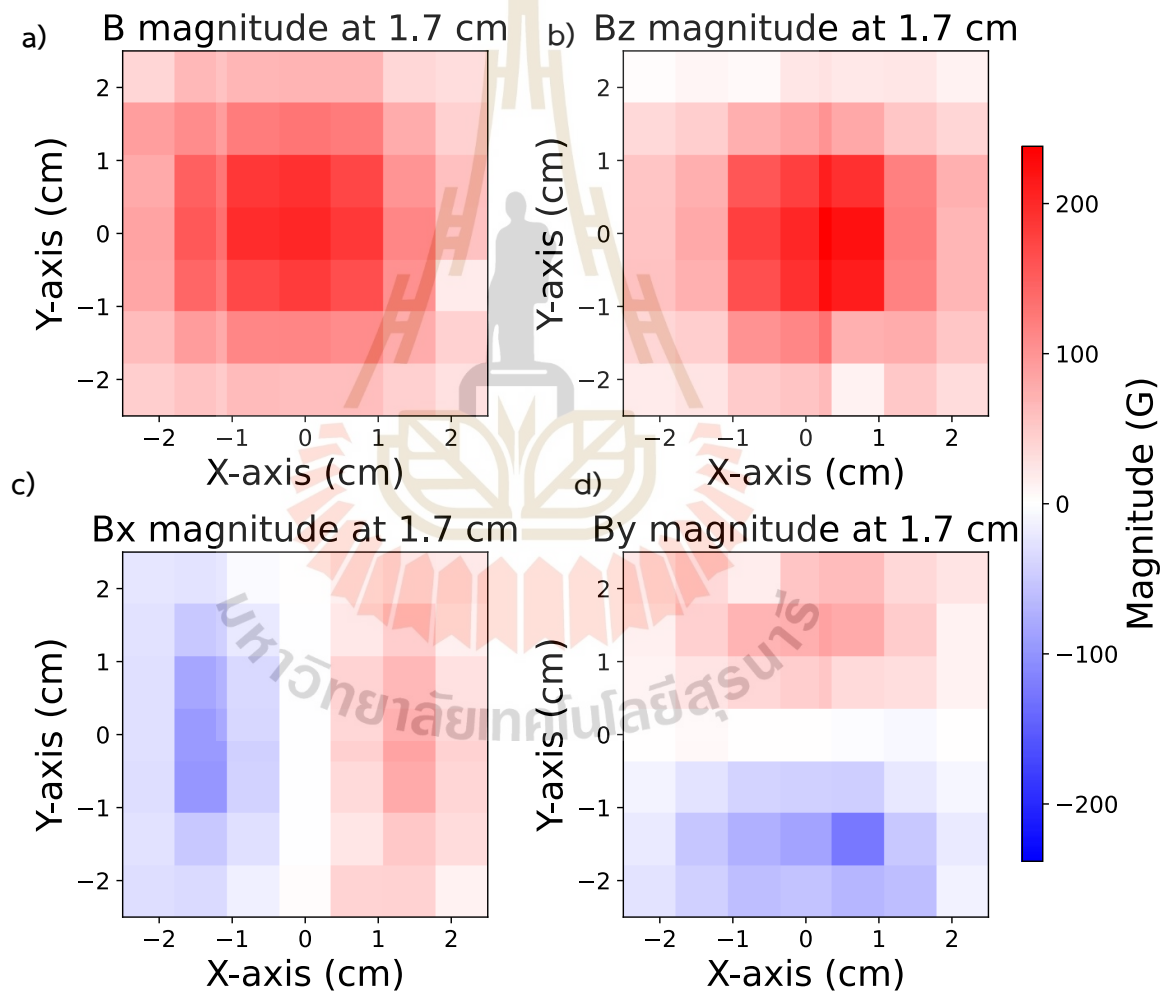


Figure 4.10 In this figure represent magnetic field gradient above the NV center at 1.7 cm. Each picture present magnetic field in cartesian coordinate. a) B_{total} b) B_z , c) B_y , d) B_x .

The individual field components— B_z , B_y and B_x —provide directional insight into the magnetic field vector. At the central position, the field is predominantly oriented along the z-axis (B_z), indicating that the field lines point outward from the magnet's surface. Consequently, B_x and B_y are approximately zero at the center. As the magnet is displaced from the center, the field direction shifts, resulting in non-zero x and y components. This change arises because the magnetic field is no longer perpendicular to the NV axis, allowing the NV center to detect components in all spatial directions.

Notably, along the $x = 0$ and $y = 0$ lines, the B_x and B_y components are zero, respectively, due to the symmetry of the magnetic field distribution. This behavior is consistent with theoretical expectations.

These results confirm that NV centers can effectively map the spatial variation of the magnetic field vector near the magnetic north pole, demonstrating the feasibility of high-resolution vector magnetometry.

4.6 Magnetic field direction above the NV center at 1.7 cm

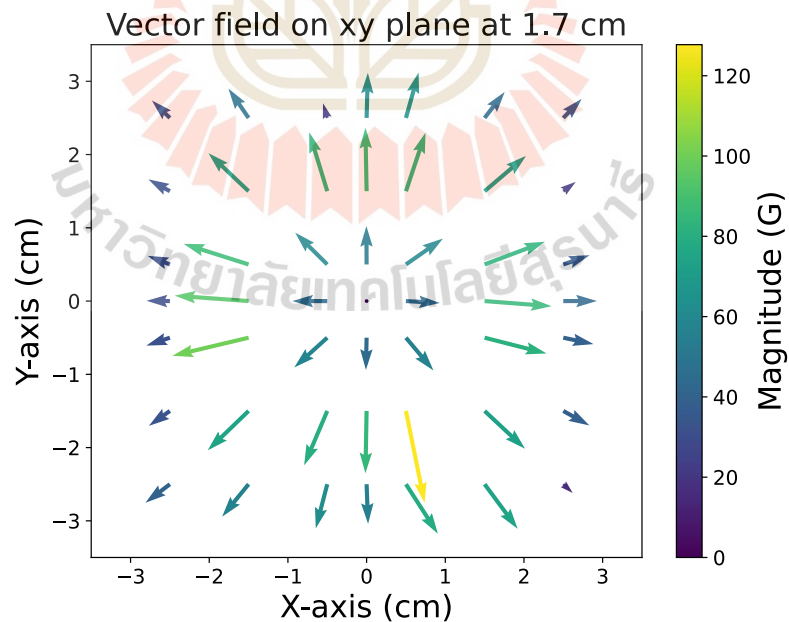


Figure 4.11 Vector field present the distribution of magnetic field in x and y direction in xy plane at 1.7 cm.

Typically, the magnetic field near the north pole of a magnet radiates outward from the magnet's surface into the surrounding space. In this context, the vector field representation captures the direction and distribution of the magnetic field within the xy plane in figure 4.11. At the center of the detection area, the magnetic field is oriented primarily along the z-axis, resulting in no visible in-plane xy components. However, immediately surrounding the center, the magnetic field vectors point outward, and the field magnitude is relatively high due to the proximity of the magnet to the NV center.

As the magnet is positioned further from the NV center, the field magnitude decreases gradually, but the vector direction continues to point outward, maintaining the radial pattern characteristic of a dipolar field.

This observed vector field behavior is consistent with the magnetic field gradient analysis discussed in Section 4.5, further validating the experimental results.

4.7 Magnetic field at 3 different heights

In this experiment, the NV center is used to demonstrate vector magnetometry at varying vertical distances from the magnet. The magnetic field at different heights interacts with the NV center differently, influencing the detected ODMR signal. Measurements were conducted at heights of 1.2 cm, 1.7 cm, and 2.2 cm above the NV center. At each height, the ODMR signal was recorded at multiple positions across the sensing area and used to reconstruct the spatial magnetic field vector.

At a height of 1.2 cm, ODMR signals near the central region could not be used in the analysis because the Zeeman splittings exceeded the frequency sweep range. B_z , B_y , and B_x

Figure 4.12 presents the calculated magnetic field gradients—total magnitude as well as the B_x , B_y , and B_z —across the three height levels. As the magnet approaches the NV center, the magnetic field gradient increases. This is particularly evident at the system's center, where the field strength is highest, and the gradient contrast is more important. The spatial extent of the strong magnetic field also becomes more localized around the center.

Similarly, both B_x and B_y increase significantly at lower heights, as shown by the higher contrast in their respective gradient maps. The behavior of B_z , however, is more complex. At positions far from the center, B_z points outward from the magnet and gradually transforms into B_x and B_y components as the field becomes less aligned with the z-axis. Near the NV center, B_z increases only around the central region, while decreasing in surrounding areas due to a shift in the magnetic field direction.

This shift represents a transition from a field pointing outward along the z-axis to one becoming more perpendicular to the NV axis. If the measurement area were extended, the z-component of the magnetic field would eventually flip direction and point downward—indicating a transition from the magnetic north pole to the south pole. These results are consistent with the expected field behavior near the magnetic poles in the xy plane.

In a vector field representation in Figure 4.13, the magnetic field near the north pole typically radiates outward from the center. The figure illustrates the magnetic field vectors at three different vertical distances in the xy plane. When the magnet is positioned farther from the NV center, the field vectors are weaker and more localized, extending only a short distance from the center. In contrast, when the magnet is positioned closer to the NV center, the magnetic field becomes stronger and its influence extends farther across the detection area, resulting in a more widely distributed vector field.

In the xz and yz planes, the vector field in Figure 4.14 is visualized along the central vertical line for three different height levels. The results show that the magnetic field direction radiates outward from the magnet, consistent with dipolar field behavior. As the NV center is positioned closer to the magnet, the field strength increases noticeably.

At a height of 1.2 cm, the magnetic field component in the z-direction near the edge of the detection area approaches zero. If measurements were extended beyond this region, the z-component of the magnetic field would reverse direction, indicating a transition from the magnetic north pole to the south pole. This polarity flip is clearly observed in both the xz and yz plane vector field plots.

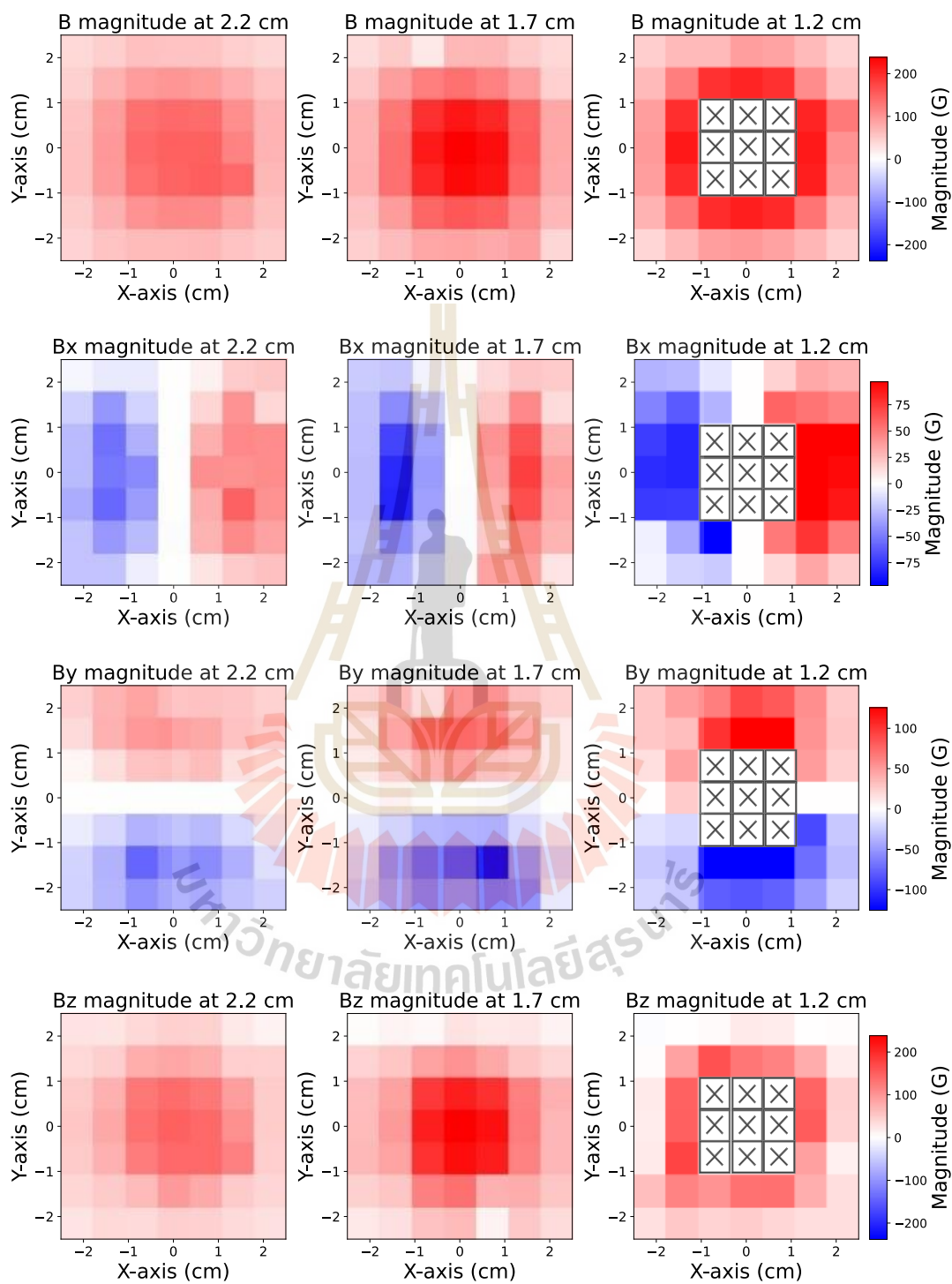


Figure 4.12 The graph represents magnetic field gradient at B_{total} , B_x , B_y and B_z at different height above the NV center. At 1.2 cm, the cross present unmeasured area.

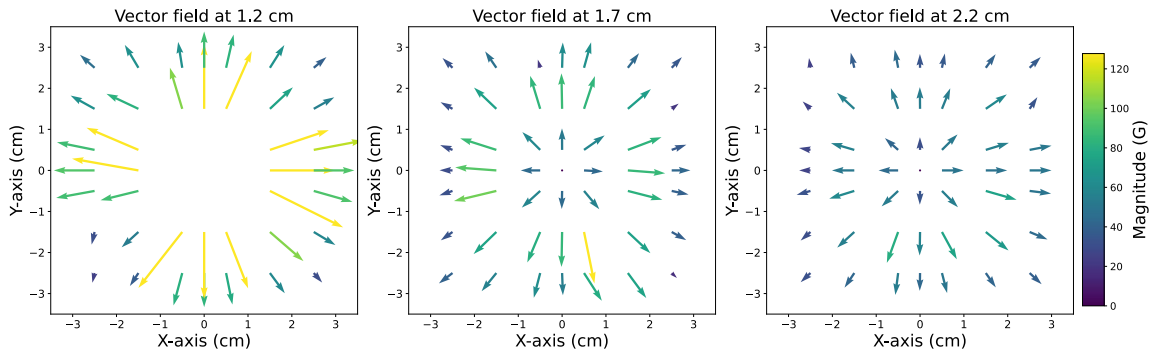


Figure 4.13 The graph represents vector field of magnetic field at the different heights above the NV center in xy plane.

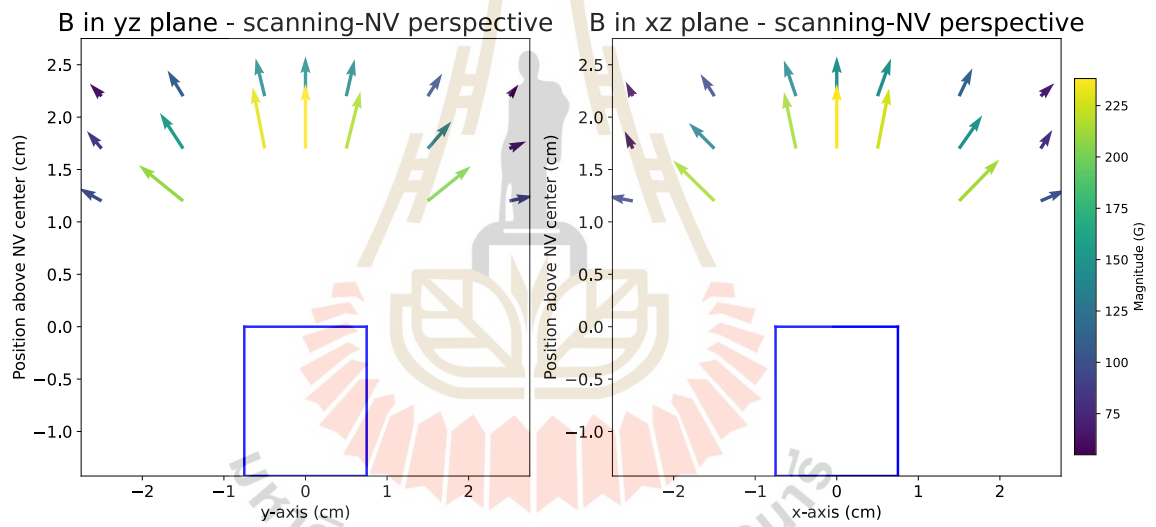


Figure 4.14 The graph represents magnetic field in yz and xz plane at the central line of y and x axis.

CHAPTER V

CONCLUSION

This thesis investigates measuring the magnitude and orientation of magnetic fields on the quantum diamond sensor with magnetic field calculations. The calculation involves distinguishing field characteristics from ODMR signals executed using three different instruments controlled by a Pulse Blaster unit and mapping unknown magnetic field vectors oriented in the direction of the North Pole.

The experimental setup aims to resolve adjacent Gaussian peaks characterized by their full width at half-maximum (FWHM), with the narrowest recorded FWHM being approximately 26 MHz in Figure 5.1. The calculation finds magnitude from 0 to 200 G in Figure 4.10 and distinguishes the ODMR signal with the smallest different angles at 2 degrees, like in Figure 4.5. The frequency sweeping program utilizes the built-in functionality of a microwave generator and integrates ODMR parameters for instrumental control and pulse duration respectively. The setup enables real-time magnetic field monitoring, capturing 200 data points every 5 seconds. However, several limitations were identified. First, a delay in frequency response from the microwave generator leads to discrepancies between the set and recorded values. Second, latency of the ODMR parameter detection process results in fewer detected data points than expected.

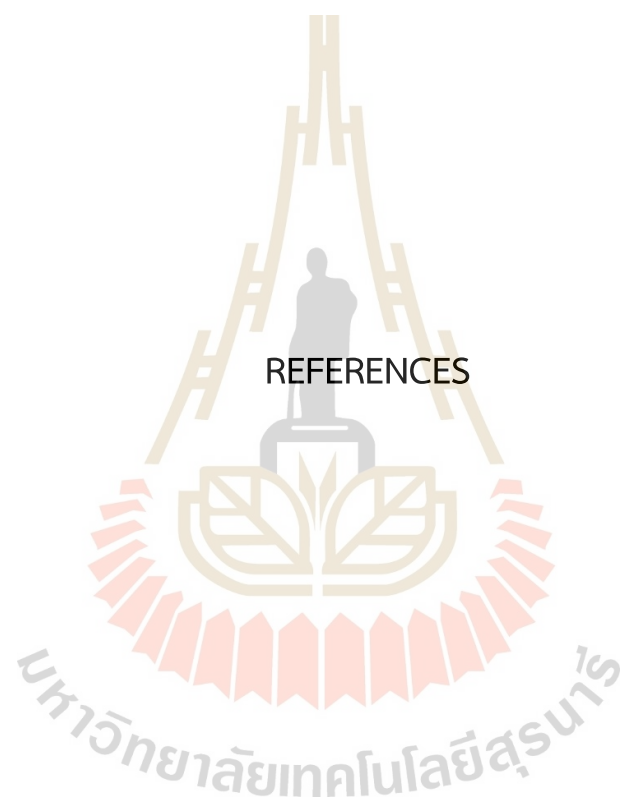
Magnetic field calculation and simulation program were developed to determine both the magnitude and orientation of magnetic fields from raw experimental data. Validating reference data indicates that the calculated results are consistent with expected values, demonstrating the system's ability to accurately resolve vector components of the magnetic field.

Importantly, the employing NV centers performs vector magnetometry by moving the magnet relative to a fixed sensor. The mapping procedure reconstructs the magnetic

field vector components— B_{total} , B_x , B_y , and B_z —in the xy plane, allowing for visualization of magnetic field gradients and directions at three distinct levels of measurement resolution.

In addition, system improvement remains possible. The system lacks automation in processes such as magnet positioning and selection of intercepts of calculated results, resulting in time-consuming repetitions. Additionally, the use of a half-wave plate (HWP) to identify NV axes via polarization is possible for the system but labeling errors and uncontrolled constraints degrade calculation accuracy. Finally, the absence of calibration parameters requires that the system be manually calibrated prior to experimentation to ensure proper configuration of critical sweeping variables.

The proposed setup has potential applications in a variety of domains, including direct current (DC) magnetic field sensing, nuclear magnetic resonance (NMR), magnetic resonance imaging (MRI), and biological sensing. Moreover, the platform offers an accessible experimental framework for educational purposes in quantum sensing and introductory quantum mechanics laboratory instruction.



REFERENCES

REFERENCES

- Acosta, V. M., Bauch, E., Ledbetter, M. P., Santori, C., Fu, K.-M., Barclay, P. E., Beausoleil, R. G., Linget, H., Roch, J. F., and Treussart, F. (2009). Diamonds with a high density of nitrogen-vacancy centers for magnetometry applications. *Physical Review B*, *80*(11), 115202.
- Alegre, T. P. M., Santori, C., Medeiros-Ribeiro, G., and Beausoleil, R. G. (2007). Polarization-selective excitation of nitrogen vacancy centers in diamond. *Physical Review B*, *76*(16).
- Ambal, K., and McMichael, R. D. (2018). Locking and Tracking Magnetic Resonance Spectra of NV-Center for Real-time Magnetometry using a Differential Photon-Rate Meter. arXiv preprint arXiv:1808.05580.
- Barry, J. F., Schloss, J. M., Bauch, E., Turner, M. J., Hart, C. A., Pham, L. M., and Walsworth, R. L. (2020). Sensitivity optimization for NV-diamond magnetometry. *Reviews of Modern Physics*, *92*(1), 015004.
- Bucher, D. B., Aude Craik, D. P., Backlund, M. P., Turner, M. J., Ben Dor, O., Glenn, D. R., and Walsworth, R. L. (2019). Quantum diamond spectrometer for nanoscale NMR and ESR spectroscopy. *Nature Protocols*, *14*(9), 2707-2747.
- Chen, B., Hou, X., Ge, F., Zhang, X., Ji, Y., Li, H., Qian, P., Wang, Y., Xu, N., and Du, J. (2020, Nov 11). Calibration-Free Vector Magnetometry Using Nitrogen-Vacancy Center in Diamond Integrated with Optical Vortex Beam. *Nano Lett*, *20*(11), 8267-8272.
- Childress, L., Gurudev Dutt, M., Taylor, J., Zibrov, A., Jelezko, F., Wrachtrup, J., Hemmer, P., and Lukin, M. (2006). Coherent dynamics of coupled electron and nuclear spin qubits in diamond. *Science*, *314*(5797), 281-285.
- DeVience, S. J., Pham, L. M., Lovchinsky, I., Sushkov, A. O., Bar-Gill, N., Belthangady, C., Casola, F., Corbett, M., Zhang, H., and Lukin, M. (2015). Nanoscale NMR spectroscopy and imaging of multiple nuclear species. *Nature nanotechnology*, *10*(2), 129-134

- Gaebel, T., Domhan, M., Wittmann, C., Popa, I., Jelezko, F., Rabeau, J., Greentree, A., Praver, S., Trajkov, E., and Hemmer, P. R. (2006). Photochromism in single nitrogen-vacancy defect in diamond. *Applied Physics B*, 82, 243-246.
- Guarina, L., Calorio, C., Gavello, D., Moreva, E., Traina, P., Battiato, A., Ditalia Tchernij, S., Forneris, J., Gai, M., and Picollo, F. (2018). Nanodiamonds-induced effects on neuronal firing of mouse hippocampal microcircuits. *Scientific Reports*, 8(1), 2221.
- Haque, A., and Sumaiya, S. (2017). An overview on the formation and processing of nitrogen-vacancy photonic centers in diamond by ion implantation. *Journal of Manufacturing and Materials Processing*, 1(1), 6.
- Joshi, K. R., Nusran, N. M., Tanatar, M. A., Cho, K., Meier, W., Bud'ko, S., Canfield, P., and Prozorov, R. (2019). Measuring the lower critical field of superconductors using nitrogen-vacancy centers in diamond optical magnetometry. *Physical Review Applied*, 11(1), 014035.
- Levine, E. V., Turner, M. J., Kehayias, P., Hart, C. A., Langellier, N., Trubko, R., Glenn, D. R., Fu, R. R., and Walsworth, R. L. (2019). Principles and techniques of the quantum diamond microscope. *Nanophotonics*, 8(11), 1945-1973.
- Li, M., Zhang, Q., Kong, X., Li, Z., Yang, Z., Zhao, S., Qin, Z., Kong, F., Chen, S., and Su, J. (2024). All-Optical Thermometry Monitoring Biochemical Kinetics with NV Centers in Diamond. *Advanced Quantum Technologies*, 7(3), 2300293.
- Liu, K. S., Henning, A., Heindl, M. W., Allert, R. D., Bartl, J. D., Sharp, I. D., Rizzato, R., and Bucher, D. B. (2022). Surface NMR using quantum sensors in diamond. *Proceedings of the National Academy of Sciences*, 119(5), e2111607119.
- Liu, Z., Zheng, D., Fu, J., Tang, C., Liu, Y., Wang, H., Li, Y., Qin, L., Wen, H., and Li, Z. (2024). Integrated NV (Nitrogen Vacancy) Vector Magnetometer in Real-time Utilizing Frequency-hopping Method. *IEEE Sensors Journal*.
- Maertz, B., Wijnheijmer, A., Fuchs, G., Nowakowski, M., and Awschalom, D. (2010). Vector magnetic field microscopy using nitrogen vacancy centers in diamond. *Applied Physics Letters*, 96(9).

- Mamin, H., Kim, M., Sherwood, M., Rettner, C., Ohno, K., Awschalom, D., and Rugar, D. (2013). Nanoscale nuclear magnetic resonance with a nitrogen-vacancy spin sensor. *Science*, *339*(6119), 557-560.
- McGuinness, L. P., Yan, Y., Stacey, A., Simpson, D. A., Hall, L. T., Maclaurin, D., Prawer, S., Mulvaney, P., Wrachtrup, J., and Caruso, F. (2011). Quantum measurement and orientation tracking of fluorescent nanodiamonds inside living cells. *Nature nanotechnology*, *6*(6), 358-363.
- Miller, B. S., Bezinge, L., Gliddon, H. D., Huang, D., Dold, G., Gray, E. R., Heaney, J., Dobson, P. J., Nastouli, E., and Morton, J. J. (2020). Spin-enhanced nanodiamond biosensing for ultrasensitive diagnostics. *Nature*, *587*(7835), 588-593.
- Mosavian, N., Hubert, F., Smits, J., Kehayias, P., Silani, Y., Richards, B. A., and Acosta, V. M. (2024). Super-resolution diamond magnetic microscopy of superparamagnetic nanoparticles. *ACS Nano*, *18*(8), 6523-6532.
- Müller, C., Kong, X., Cai, J.-M., Melentijević, K., Stacey, A., Markham, M., Twitchen, D., Isoya, J., Pezzagna, S., and Meijer, J. (2014). Nuclear magnetic resonance spectroscopy with single spin sensitivity. *Nature Communications*, *5*(1), 4703.
- Perdriat, M., Pellet-Mary, C., Huillery, P., Rondin, L., and Hétet, G. (2021). Spin-mechanics with nitrogen-vacancy centers and trapped particles. *Micromachines*, *12*(6), 651.
- Turner, E., Wu, S.-H., Li, X., and Wang, H. (2022). Real-time magnetometry with coherent population trapping in a nitrogen-vacancy center. *Physical Review A*, *105*(1), L010601.
- Wang, Z., Kong, F., Zhao, P., Huang, Z., Yu, P., Wang, Y., Shi, F., & Du, J. (2022). Picotesla magnetometry of microwave fields with diamond sensors. *Science Advances*, *8*(32), eabq8158.
- Wood, A., Lozovoi, A., Goldblatt, R., Meriles, C., and Martin, A. (2024). Wavelength dependence of nitrogen vacancy center charge cycling. *Physical Review B*, *109*(13), 134106.

CURRICULUM VITAE

Name: Napoom Thooppanom

Date of Birth: 16 September 1999

Place of Birth: Chaiyaphum, Thailand

Educations:

- 2018-2022: School of Physics, Science, Suranaree University of technology, Nakhon Ratchasima, Thailand (Bachelor of Science)
- 2022-2025: School of Physics, Science, Suranaree University of technology, Nakhon Ratchasima, Thailand (Master of Science)

Publication:

Thooppanom, N., Yodsungnoen, R., Sapermsap, N., Sangtawesin, S., 2025. Real Time Vector Magnetometry with Quantum Diamond Sensor. *Journal of Physics: Conference Series*, **2934**, 012022

Grants and Fellowship:

Development and Promotion of Science and Technology Talents Project (DPST)

